MOLECULAR DOCKING, ATOM-BASED 3D-QSAR, MOLECULAR DYNAMICS AND PHARMACOPHORE MODELLING INVESTIGATIONS FOR SARS COV-2 MPRO

Kannan R[1], Kalirajan R[2]* Srikanth J[2], Kavinkumar MC[3,4], Krishna SS[2], Dhinesh Kumar M[2]

[1]Department of Pharmacology, St.Johns College of Pharmaceutical Sciences & Research, Kattappana, Idukki, Kerala-685515, India.
[2]Department of Pharmaceutical Chemistry, JSS College of Pharmacy, (A Constituent college of
JSS Academy of higher education & Research- deemed University), Ooty – 643001, the Nilgiris, Tamilnadu, India.
[3]Department of Pharmaceutical Chemistry, Vellalar College of Pharmacy, Maruthi Nagar, Thindal, Erode, Tamilnadu – 638012, India.
[4]Affiliated by The Tamil Nadu, Dr.M.G.R. Medical University, Chennai, Tamil Nadu, India.

***Correspondence**
Dr. Rajagopal Kalirajan
E-mail: rkalirajan@jssuni.edu.in

Abstract

The cause of COVID-19 is SARS-CoV-2, a single-stranded RNA virus from the beta coronavirus genus. Developing direct-acting antivirals targeting SARS-CoV-2 is crucial. Molecular Mechanics/Generalized Born Surface Area (MM/GBSA) is used in pharmacophore-based pharmaceutical research to calculate ligand-receptor binding free energy. The Mprotease (Mpro) enzyme is a prime target for COVID-19 medicines. A 3DQSAR model, AADHR.187, was created using 107 Mpro inhibitors from SARS-CoV-2. The model yielded strong prediction coefficients (R2 = 0.98 for training and R2 = 0.86 for testing) and a cross-validated correlation value (Q2 = 0.976). Enrichment studies validated the model's utility, and a diverse ten-compound exterior test set confirmed its reliability. Contour plot analysis of the model revealed molecular characteristics required for Mpro inhibition. Precise docking studies emphasized the importance of ionic and hydrogen bonding interactions in Mpro-ligand binding. Binding free energy calculations supported the binding affinity of inhibitors. Molecular dynamics modelling showed that inhibitor 34 effectively bound to Mpro's active site (protein ID: 6XQS) over 100 nanoseconds. Pharmacophore-based high-throughput virtual screening, using model AADHR.187, led to identifying three new compounds with favourable ADME properties and strong binding affinities as potential SARS-CoV-2 Mpro inhibitors. These findings hold promise for developing effective COVID-19 treatments.

Keywords: SARS-CoV-2, Mpro inhibitors; Pharmacophore model, molecular docking, MMGBSA, Molecular dynamics.

1. Introduction

Severe Acute Respiratory Syndrome coronavirus 2 (SARS-CoV-2) is an illness that is brought on by the corona viruses SARS-CoV-2, correspondingly. It has four parts envelope protein, spike protein, RNA and lipid membrane. Numerous individuals have died as a result of its role in widespread pulmonary illness epidemics. These infections are believed to have emerged from bats and are quite dangerous to people[1]. According to the virus's fast global transmission, a pneumonia epidemic in Wuhan (China) in December 2019 drew a lot of media notice. The new coronavirus SARS-CoV-2 has now been discovered as the previously unidentified source of the infection (formally renamed as COVID-19)[2].It was evident from the early genomic analyses that SARS-CoV-2-genome was organized similarly to SARS-CoV2. Since both viruses' spike proteins have comparable three-dimensional shapes, it was rapidly shown in vitro and utilizing molecular science that both viruses may employ the physical angiotensin-converting enzyme (ACE) as a cell membrane interface. SARS-CoV-2, though, differs from SARS-CoV-2 in two key aspects[3]. Figure 1 shows the parts of SARS-CoV-2.

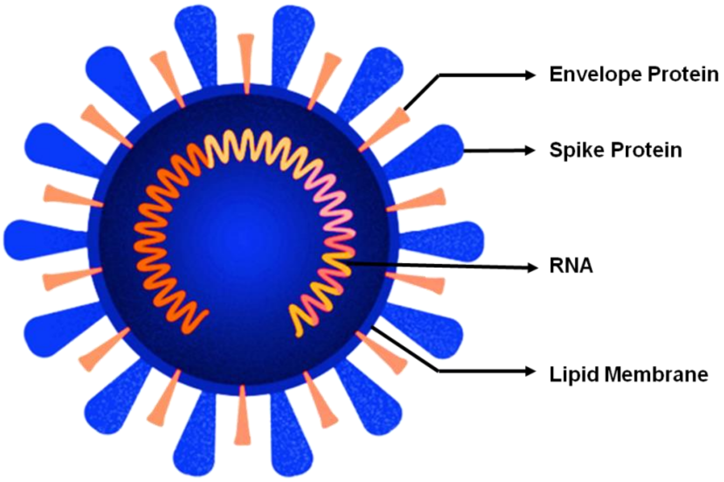

Fig. 1. Parts of SARS-CoV-2

Initially, the connection of the SARS-CoV2 and SARS-CoV-2 spike proteins to the individual ACE receptor is mediated by six amino acid residues in the receptor-binding region (RBR) of the spike protein. However, among SARS-CoV-2, amino acids at five of the six locations were different. Significantly, these variations led to SARS-CoV-2 having a greater holding avidity to the human ACE2 region and may have helped explain why SARS-CoV-2 was more contagious than SARS-CoV2[4].

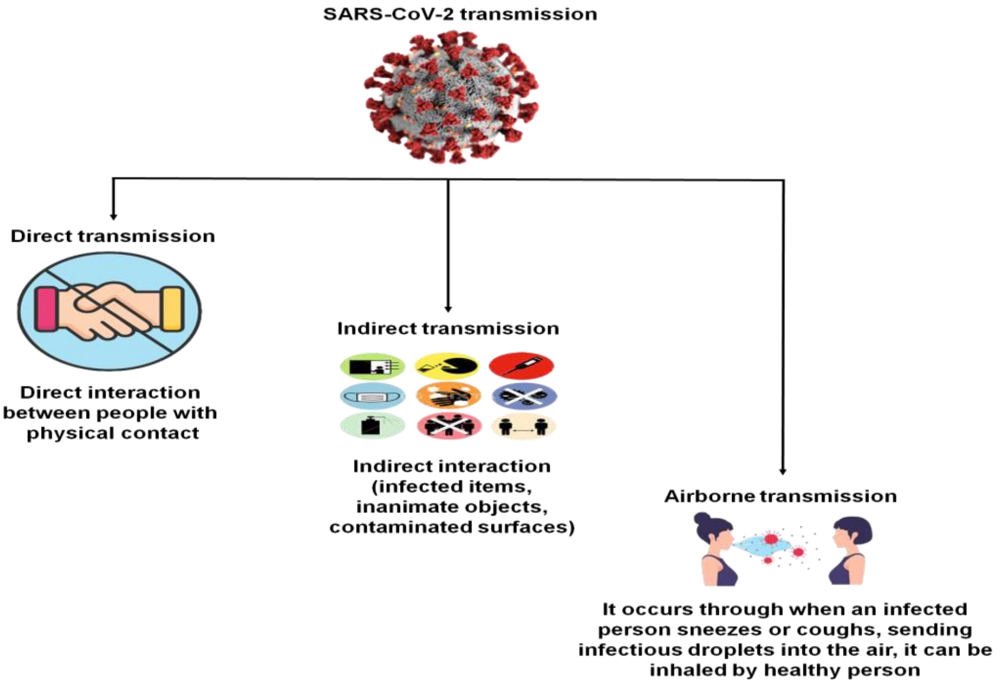

Fig.2. Transmission of SARS-CoV2

Figure 2 shows the transmission of SARS-CoV2. It is essential to comprehend how viruses spread in order to design efficient management options. Direct interaction between people, indirect interaction through infected items (fomites), and airborne transfer through raindrops and particles have been shown to be the three main ways that this virus spreads[4]. When a person is sick, breathing fluids and inhalation particles released when talking, breathing, or spitting may directly contaminate a fomite or another person[5]. Aerosol molecules may hang in the atmosphere for minutes to hours as drops fall and attach onto surfaces. Interaction with the fomite and later encounter with body parts where a virus may enter the body results in indirect fomite-mediated transfer to a new person victim[6]. One to fifty seconds may pass during a contact. Furthermore, virus molecules may be spread to a surface by touching infected skin [7]. The M protease, the most prevalent basic component in SARS-CoV-2, bridges the wall bilayer, exposing a lengthy COOH terminal (intracellular region) within the virion and a short NH2-terminal region beyond the virus[8,9]. All other structure molecules can connect to the M protease. By maintaining the N protease combination within the interior virion, interaction with M protease aids in stabilizing N protease and encourages the finalization of viral construction. Variations might affect how the viruses connect to and enter the host cell since the M protease works in conjunction with the S protease. The virus's S protease has been glycosylated, and this alteration may help the virus evade the immunological system[10].Figure 3 depicts the structure of M-Protease.

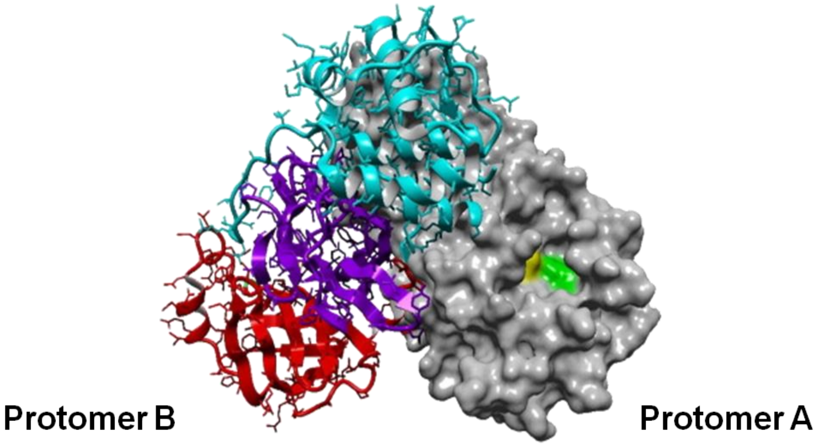

Fig.3. Structure of M-Protease

A pharmacophore (PH) is a chemical framework that specifies the essential properties that give rise to a particle's physiological action. To better comprehend how ligand-protein combinations work, pharmacophore designs are created. It may be used to find novel compounds that meet the pharmacophore criteria and are thus anticipated to be effective. If the targeting architecture is not known, pharmacophore designs may be created utilizing the molecular details of the effective ligands which bind to the receptor. This method is referred to as ligand-based pharmacophore simulation. When the target's form is known, pharmacophore modeling may be created utilizing the target's physical characteristics. This is referred to as a structure-based pharmacophore simulation technique[11].The process of discovering new drugs is difficult and necessitates the use of diverse methodologies. The drug development process has incorporated pharmacophore simulation at many phases. Evaluation, docking, drug targeting identification, and ligand analysis are the main usage domains. Many pharmacophore simulation applications are being used. The client should carefully choose the best application for the intended use. To find related ligands with established modes of action, chemoinformatics-based resemblance discovery techniques are used. Nonetheless, pharmacophore simulation may be used in ways apart than finding compounds using a pharmacophore search. The objective here is to identify the pharmacophore model that would be appropriate for the molecule under research, which might be the query[12]. The U.S. Food and Drug Administration (FDA), a division of the Cabinet of Healthcare and Human Services, safeguards the people's education by ensuring the integrity, efficacy, and quality of pharmaceuticals for usage in people and animals, medical equipment, and vaccinations[13]. The organization is in charge of supervising tobacco goods as well as the health and stability of the country's food production, perfumes, nutritional additives, and devices that emit digital radiation. The FDA has authorized a wide variety of pharmacological treatments that target various biological processes and disease-related processes[14].

2. Materials and Methods

2.1. Biological data collection (6XQS)

The Phase component was used to carry out atom-based 3D QSAR and pharmacophore modeling for 107 inhibitors. It is now possible to perform pharmacophore modelling and 3D library querying as essential steps in the lead identification, lead refinement, creation of the structure-activity connection, and creation of the 3D modeling processes. To create the pharmacophore modeling panel of the Phase modules, the generated compounds with their corresponding biological performance values were input. Although the other substances were highly active, a pharma plan column was designated as actives with a cutoff of pMIC > 5.8 inactive with a cutoff of pMIC 3.5. Moreover, the default parameters were utilized, and a maximal of 100 conformers and 10 conformations per rotational bond were formed. A maximum of one orientation per ligand was kept when amide bonds' configurations were changed. Utilizing the Automatic Random Selection function in the PHASE programme, 107 atoms were arbitrarily picked as the training set and 19 as the training dataset. Finally, while maintaining a tolerance for 1 pharmacophore matching, pharmacophore sites for these substances were established. By systematically varying a number of locations and the quantity of relevant active chemicals, hypotheses were produced. Utilizing the six chemical characteristics of Phase's default set, typical pharmacophores with five sites were created. Finally, while maintaining a tolerance for 1 pharmacophore matching, pharmacophore sites for these substances were established.

2.2. 3D-QSAR research and pharmacophore model

We created 3D-QSAR and pharmacophore concepts using Phase depending on the 107 MPro compounds. The phase's Develop Pharmacophore Model component imported the molecular layouts along with their corresponding MI05 values, and dithrimidil was used to geometrically improve them[15]. ConfGen (v3.5) was used to investigate the conformational space; a maximum of 1000 conformers per molecule were created with 100 conformers per rotational bond. For the solvation therapy, a dielectric that changes with distance was used. For active compounds, a threshold of MI05 6.30 was set, while for inactive compounds, MI05 4.57. The remaining molecules were considered to be somewhat active. 91 compounds were chosen as the training set components based on their diverse structural makeup and broad range of MI05 values (3.838 to 663 M). The remaining nine compounds were included as test set compounds because they had enough structural variety and well-distributed physiological data (IC50 range: 4.096 to 7.455 M). The six pharmacophoric properties that were accessible in Phase were used to produce pharmacophoric locations for all of the ligand conformers that were produced. A total of 11 different combinations of pharmacophoric sites were created, with a minimum of three and a maximum of five being used. Moreover, five-point pharmacophore hypotheses with 1 matching tolerance that match to all active ligands (pIC50 6.30) were produced. Two units were chosen as the minimal intersite distances between two characteristics. Using the site rating, surviving score, surviving inactives, volumetric rank, matrix score, number of connections, and energy terms, the top five produced hypotheses were chosen. The MI05 is high active compound and dithrimidil is least active compound[16].Figure 4depicts the proposed workflow. AADHR.187, a pharmacophore with five features that match the data the best, was chosen for further investigation. The “van der Waal's” modeling of the training and testing set ligands was aligned depending on the derived best model AADHR.187 Table 1.

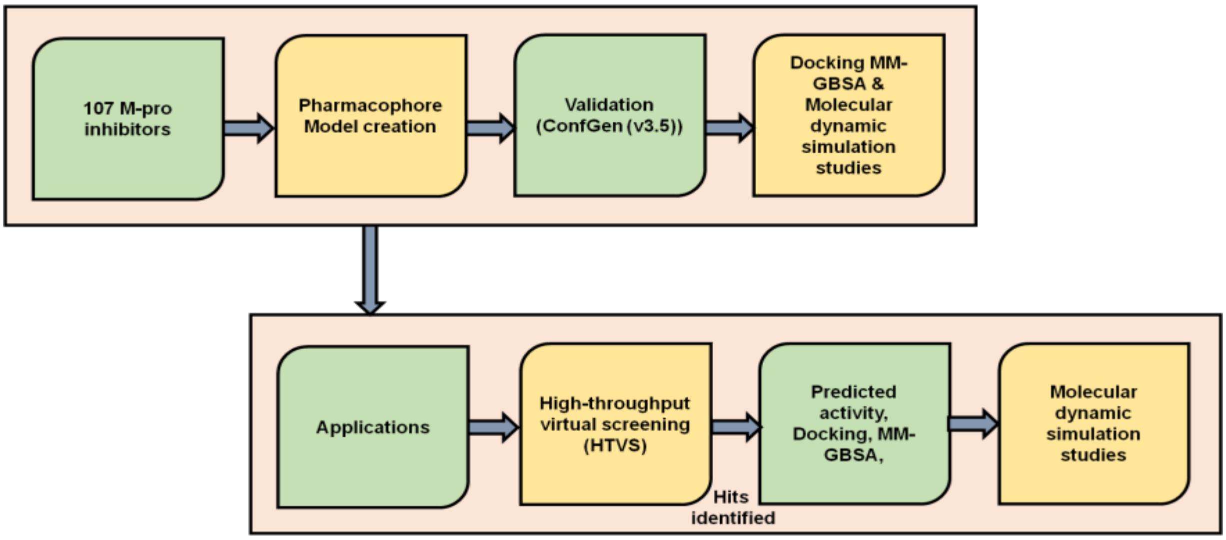

Fig.4. Proposed workflow

Table 1. Score for the different parameters of the best five generated hypotheses

Hypothesis	Survival – inactive	Posthoc	Site	Volume	Inactive	Survival	Vector	Energy	Matches	Activity
AADHR.133	1.103	3.039	0.75	0.639	1.522	3.049	0.884	0.598	09	5.663
AADHR.201	1.142	3.192	0.77	0.612	1.352	3.192	0.921	0.597	09	6.386
AADHR.187	1.166	3.273	0.81	0.653	1.117	3.273	0.924	0.349	09	6.833
AADHR.147	1.142	3.192	0.74	0.618	1.139	3.192	0.923	0.497	09	6.347
AADHR.195	1.741	3.042	0.74	0.640	1.343	3.189	0.876	0.583	09	6.231

Also, utilizing the seven compounds in the aligned training dataset, a quantitatively relevant atom-based 3D-QSAR framework was created using partial least-squares (PLS) analysis[17]. Up to four PLS variables, a rise in statistical relevance and predictability Table 2&Table 3: Enrichment factor (EF) values of the generated 3D-QSAR models.

Table 2: Summary of 3D-QSAR PLS statistical results of the best generated model AADHR.187

PLS	SD	Pearson-R	F	Stability	R^2	RMSE	Q^2	P
1	0.468	0.701	87.55	0.618	0.766	0.466	0.652	5.84e-10
2	0.193	0.887	297.43	0.710	0.960	0.445	0.684	1.23e-19
3	0.156	0.887	325.58	0.773	0.978	0.294	0.756	3.76e-21
4	0.120	0.894	417.36	0.780	0.986	0.210	0.798	8.44e-23

Table 3: Enrichment factor (EF) values of the generated 3D-QSAR models

Pharmacophore model	ROC	AUC	RIE
AADHR. 195	0.79	0.89	6.28
AADHR. 201	0.93	0.90	6.96
AADHR. 187	1.01	0.96	8.67
AADHR. 133	0.74	0.88	6.30
AADHR. 147	0.95	0.92	7.79

The matching of active and inactive ligands with the created model AADHR.187 is shown in Figures 1c and 1d. 9 test set ligands that weren't utilized while creating the model but were utilized to verify it were employed to do so. Utilizing this approach, the fitness scores of all ligands were evaluated. Moreover,[18] used the model to forecast the behavior of the compounds in the exterior testing sample E1-E10. To continue study the structure-activity connection of the ligands towards the MPro enzyme, contour plots were created and then evaluated (Fig. 5 a–d).

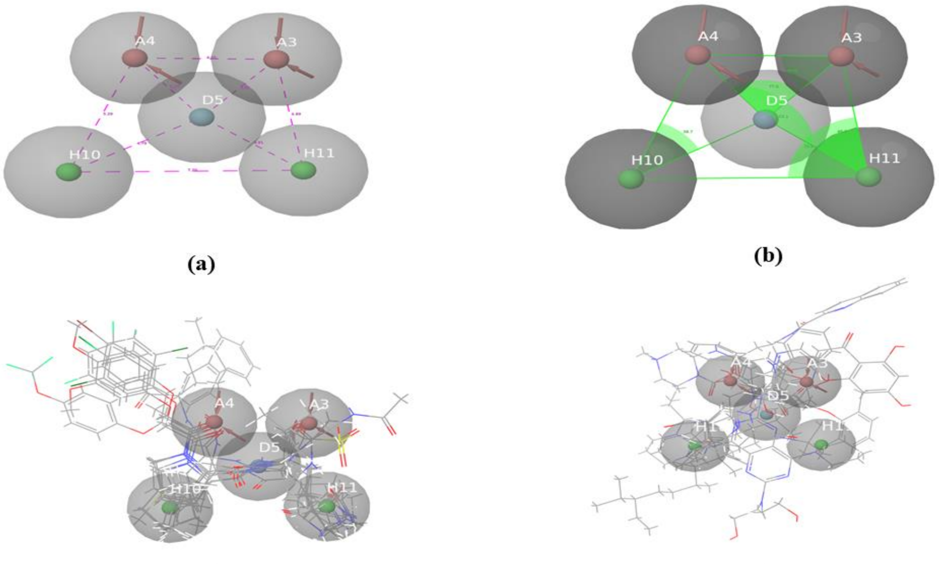

(a) (b)

(c) (d)

Fig.5. shows the inter-site (a) distances in units of and (b) angles between the pharmacophoric sites for the pharmacophore model AADHR.187 (c) Aligning active molecules on the pharmacophore model that was developed (d) Aligning inactive molecules on the pharmacophore model that was produced.

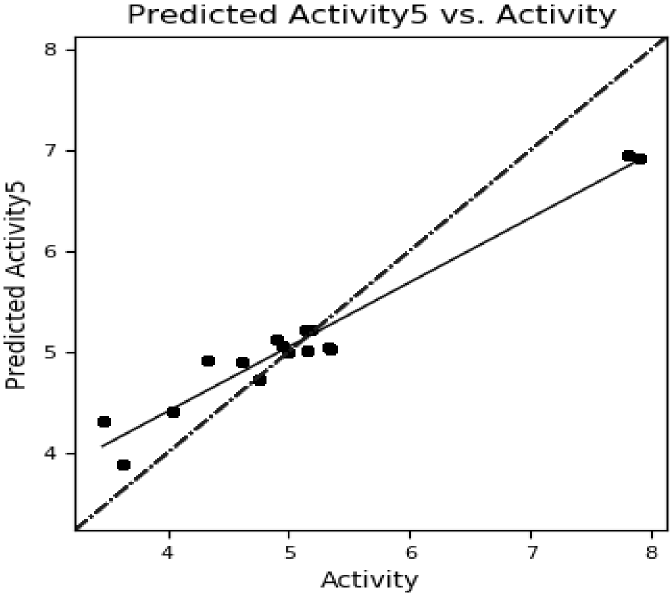

Fig.6. Depicts scatter graphs comparing test performance that was forecasted against actual movement

2.3. Molecular docking

The protein database bank's 3D structures of the MPro protein in association with the benzimidazol-2-yl-3-ethylurea analog was obtained, and the Protein Processing Wizard was used to prepare it (Epik v3.5). At pH 7.02.0, hydrogen bonds were removed from action site water particles with less than three hydrogen bonds and added[19]. Utilizing the Prime, the protein structure's fractures were patched together and the side chain atoms that were missing were inserted (v4.3). Using the OPLS3 force field, the energy of the protein architecture was reduced until the RMSD of the heavy atoms converged to 0.3. The Ramachandran plot shows that 99.20% of the compounds are in the areas that are most preferred, and none of the non-glycine compounds are in the sections that are prohibited[20].Moreover, a grid box was created surrounding the active site, which had a 10 radius around the co-crystallized ligand. Grid-based ligand docking with energetics (Glide v7.5) in extra-precision (XP) mode was used to dock the low energy structures of all ligands into the catalytic site [19]without the use of any restrictions (Fig. 7a–d). Depending on the Glide score (Gscore) function, Glide energy, and Glide emodel, the optimal docked position for each ligand was determined. The 30 ns molecular dynamics simulation was done using the 38/6XQS complex's optimal posture.

Table 4: Molecular docking for SARS CoV 2 Mpro

Compound code	docking_score	glide_evdw	glide_ecoul	_glide_energy	_glide_emodel
Disulfiram.mol	-9.98337	-50.3824	-8.22728	-58.6097	-90.1212
Atazanavir.mol	-9.7664	-32.9714	-10.5904	-43.5618	-61.4325
Quercetin,.mol	-9.26108	-41.2433	-17.7272	-58.9704	-71.4062
Theaflavin.mol	-9.21194	-32.1076	-13.7306	-45.8383	-67.3026
EGCG.mol	-9.21194	-32.1076	-13.7306	-45.8383	-67.3026
Amentoflavone.mol	-8.93121	-33.0662	-9.0816	-42.1478	-54.9046
dipyridamole.mol	-8.72439	-48.6883	-6.27378	-54.9621	-85.8209
beta-lapachone.mol	-8.67996	-43.3226	-10.6659	-53.9885	-64.3696
2,3,4-Trihydroxy-4â€™-ethoxybenzophenone.mol	-8.63669	-36.1603	-5.72354	-41.8838	-59.8087
Trihexyphenidyl.mol	-8.56848	-58.8119	-13.8509	-72.6628	-118.219
Baicalein.mol	-8.42196	-35.6934	-4.69133	-40.3847	-52.6661
GC-376.mol	-8.34328	-45.9988	-4.62229	-50.6211	-72.1432
AMG-837.mol	-8.24509	-35.4239	-3.86723	-39.2912	-52.8655
gallocatechin gallate.mol	-8.05258	-64.7917	-7.04852	-71.8402	-110.739
Rottlerin.mol	-8.02987	-34.4261	-4.00687	-38.433	-47.4009
GC-376.mol	-7.94281	-38.7884	-13.7798	-52.5682	-74.6742
walrycin B.mol	-7.94281	-38.7884	-13.7798	-52.5682	-75.0347
Ebastine.mol	-7.70782	-53.8464	-10.5743	-64.4207	-84.7219
Sinigrin.mol	-7.67332	-32.5661	-3.59823	-36.1643	-44.931
Cimetidine.mol	-7.65122	-30.4684	-9.51448	-39.9829	-56.4454
MI-21.mol	-7.54964	-40.4733	-11.2847	-51.758	-78.1057
agaric acid.mol	-7.54716	-39.356	-7.05091	-46.4069	-67.1554
Leteonin.mol	-7.54428	-31.3305	-3.45665	-34.7872	-47.5488
NSC 95397.mol	-7.52375	-47.6586	-5.4256	-53.0842	-71.4962
Oxytetracycline.mol	-7.47718	-34.0254	-4.16399	-38.1894	-47.4204
MK-886.mol	-7.4276	-50.7444	-5.5791	-56.3235	-69.4858
MI-11.mol	-7.38098	-47.8933	-6.97442	-54.8677	-74.3151
Duloxetine.mol	-7.27808	-45.2147	-8.93701	-54.1517	-65.9302
Saquinavir.mol	-7.25297	-53.6532	-13.3271	-66.9804	-102.533
Indican.mol	-7.23177	-33.6119	-4.93995	-38.5519	-50.2979
Indirubin.mol	-7.19694	-31.5383	-9.03576	-40.574	-45.6345
MI-09.mol	-7.083	-49.1623	-7.1501	-56.3124	-67.1005
MI-23.mol	-7.01911	-42.5877	-8.29035	-50.8781	-77.1345
Aloeemodin..mol	-6.99169	-44.331	-10.3695	-54.7005	-74.4445
MI-05.mol	-6.84223	-45.7726	-8.40221	-54.1748	-67.5822
Calpain inhibitor XII.mol	-6.83757	-52.0286	-5.61065	-57.6393	-83.478
Tipranavir.mol	-6.76952	-53.4592	-7.94488	-61.4041	-82.9649

Calpain inhibitor I.mol	-6.73134	-45.9837	-2.08698	-48.0706	-61.1098
Anacardic Acid.mol	-6.71358	-40.9818	-7.90449	-48.8863	-67.7572
MI-06.mol	-6.67495	-49.998	-5.75401	-55.752	-68.8323
sepantronium bromide.mol	-6.66457	-35.433	-3.92005	-39.353	-50.634
MI-13.mol	-6.66356	-46.5788	-8.78156	-55.3604	-74.7905
Eltrombopag olamine.mol	-6.48498	-46.3073	-5.17413	-51.4814	-73.6089
Montalukast.mol	-6.47082	-30.3652	-1.12874	-31.4939	-45.8976
SU 16f.mol	-6.43594	-31.9768	-7.36938	-39.3462	-53.2442
Shikonin.mol	-6.2768	-35.7398	-8.79705	-44.5369	-60.5664
LLL-12.mol	-6.26414	-39.1003	-1.48855	-40.5888	-46.2312
MG-149.mol	-6.09265	-50.2279	-4.18567	-54.4135	-81.6616
Bepridil.mol	-6.08734	-39.2321	-2.17622	-41.4083	-61.6976
Rimonabant.mol	-6.08695	-38.9837	-3.20023	-42.184	-59.8919
MAC-13985.mol	-6.03546	-39.6108	-0.1512	-39.762	-46.2713
Pimozide.mol	-6.03335	-59.6099	-8.0454	-67.6552	-101.302
Itraconazole.mol	-5.96658	-49.7015	-5.70484	-55.4063	-79.0138
MK 0893.mol	-5.93331	-40.5868	-1.58562	-42.1725	-56.5942
Ebselen.mol	-5.87032	-39.0086	-9.67883	-48.6874	-63.2519
Z-FA-FMK.mol	-5.86172	-33.5044	-2.63808	-36.1425	-47.0677
Carmofur.mol	-5.851	-60.0848	-1.85704	-61.9418	-92.0758
CAY-10581.mol	-5.79249	-31.6373	-2.04891	-33.6862	-45.3128
Evans blue.mol	-5.69862	-56.0438	-3.92067	-59.9644	-81.6628
Montalukast.mol	-5.65679	-59.3548	-5.87781	-65.2326	-86.5008
Metixene.mol	-5.64943	-32.8796	-2.78971	-35.6693	-48.5085
ivermectin.mol	-5.63666	-31.4498	-11.1027	-42.5525	-43.456
Adomeglivant.mol	-5.55142	-51.7855	-7.67732	-59.4628	-81.3733
Daidzein.mol	-5.49556	-41.1431	-1.66323	-42.8063	-60.7199
Calpain inhibitor II.mol	-5.43825	-38.8342	-0.31508	-39.1493	-55.8835
Sertaconazole.mol	-5.34396	-44.1968	-1.26861	-45.4654	-64.7134
Bronopol.mol	-5.29472	-26.4566	-4.95706	-31.4137	-38.8902
Valacyclovir hydrochloride.mol	-5.28953	-22.7226	-4.43667	-27.1592	-32.0834
paritaprevir.mol	-5.27633	-34.3098	0.649617	-33.6602	-44.4437
untitled.mol	-5.17664	-71.8859	-7.58558	-79.4715	-133.769
Zopiclone.mol	-5.17592	-28.5404	-6.4917	-35.0321	-42.6011
Clemastine.mol	-5.16003	-31.4591	-1.84237	-33.3014	-38.8909
Baicalin.mol	-5.14171	-40.9801	-3.90321	-44.8833	-64.777
SP 100030.mol	-5.04201	-22.8023	-1.01052	-23.8128	-29.6215
MAC-30731.mol	-4.97589	-23.2767	-5.85821	-29.1349	-37.7698
Vanitiolide.mol	-4.90639	-35.1989	-2.53158	-37.7305	-43.9581
Chloranil.mol	-4.9022	-17.1988	-8.20459	-25.4034	-29.2885
Tideglusib.mol	-4.83527	-31.635	-5.26175	-36.8967	-41.7024

DA-3003âˆ’1.mol	-4.66707	-30.1409	-3.61348	-33.7544	-39.4478
Hexachlorophene.mol	-4.54927	-39.877	-3.60774	-43.4848	-60.4493
MI-14.mol	-4.50361	-44.513	-6.49886	-51.0119	-68.7927
Indinavir.mol	-4.34567	-34.0435	-6.46141	-40.5049	-46.7341
Z-DEVD-FMK.mol	-4.23912	-18.1124	-3.07056	-21.183	-26.9825
PX-12.mol	-4.19741	-46.0361	-3.25898	-49.2951	-69.1419
Thimerosal .mol	-4.18667	-18.4155	-2.03692	-20.4524	-24.9809
Oxiconazole.mol	-4.16062	-57.3808	-5.90665	-63.2875	-89.727
Hydroxychloroquine.mol	-4.08955	-33.6338	-0.34691	-33.9807	-44.693
Chloroquine.mol	-4.0493	-21.784	-1.67238	-23.4564	-29.0413
Roxatidine acetate hydrochloride.mol	-4.04074	-38.7746	-1.22838	-40.003	-53.8254
GSK-3965.mol	-3.99862	-36.3663	-1.6528	-38.0191	-53.9885
GW5074.mol	-3.99275	-31.3742	-3.92942	-35.3036	-43.7504
Sulfacetamide.mol	-3.82073	-44.3231	-1.11623	-45.4394	-64.3763
Fascaplysin.mol	-3.79567	-29.019	-3.88015	-32.8992	-40.5874
Candesartan cilexetil.mol	-3.6819	-33.2201	-4.14645	-37.3666	-46.2893
Rupintrivir.mol	-3.65713	-32.6927	-5.26425	-37.957	-50.7189
ombitasvir.mol	-3.64197	-60.3477	-0.95858	-61.3063	-82.8719
epigallocatechin gallate.mol	-3.56197	-35.536	-5.93592	-41.472	-52.854
Plumbagin.mol	-3.50462	-37.0735	-8.06987	-45.1433	-56.488
Nelfinavir.mol	-3.43373	-41.4967	-1.80389	-43.3006	-54.7325
Lopinavir.mol	-3.38829	-37.5365	-4.06189	-41.5984	-58.6712
suramin.mol	-3.04717	-60.1069	-17.0357	-77.1426	-90.2509
MAC-22272.mol	-2.61058	-28.3959	-3.29817	-31.694	-41.9164
Hesperetin.mol	-2.38044	-31.039	-2.28926	-33.3282	-41.5363
Omeprazole.mol	-1.51319	-20.9538	-6.00148	-26.9553	-32.2993
3,4-Didesmethyl-5-deshydroxy-3â€™-ethoxyscleroin.mol	-1.03987	-33.8434	-5.26586	-39.1093	-50.328
Maribavir.mol	0.203271	-29.1386	-4.38385	-33.5225	-42.737

2.4 Binding free energy estimation

The “structural mechanics-generalized born square area (SM-GBSA)” approach was used to determine the binding free energy for all of the attached compounds. This method is an effective technique for correctly rating inhibitors. Utilizing Prime's local optimization function, the extra-precision attached ligand-enzyme combination architectures were eliminated (v4.3). By placing any restrictions on flexible residues, models were run utilizing input ligand partial energies. The bonding free values were calculated utilizing the MM-GBSA continuous fluid and VSGB 2.0 solvation theory with the OPLS3 force field [21,22]. Table 5 shows the MM-GBSA data.

Table 5: MM-GBSA *Binding free energy calculation*

Title	MMGBSA_dG_Bind	MMGBSA_dGCoul	rMMGBSA_dG_Bind_Hbond	MMGBSA_Lipo	MMGBSA_vdW
Z-DEVD-FMK.mol	-100.748	-51.5659	-4.40246	-0.09771	7.006759
Saquinavir.mol	-91.8881	-17.0389	-2.98542	0.759153	25.75639
Nelfinavir.mol	-88.5362	-56.8997	-2.44572	4.751211	12.64793
ombitasvir.mol	-85.0939	-49.6445	-3.72068	0.774498	19.79731
Atazanavir.mol	-80.1466	-26.2547	-2.8242	3.951764	29.42891
suramin.mol	-79.5849	87.19096	-5.66981	0.067565	13.7829
Indinavir.mol	-75.333	-11.2346	-1.63984	1.483893	33.45146
Itraconazole.mol	-72.9589	13.44095	0.674381	6.745355	6.445599
Ebastine.mol	-72.2362	-8.92092	0.198548	0.104384	7.901187
Rupintrivir.mol	-72.0668	-4.09518	-1.02191	4.200408	15.08187
MI-06.mol	-71.9196	-14.5054	-0.41631	0.434568	23.83836
Eltrombopag olamine.mol	-70.8588	-19.638	-1.62379	-0.22567	23.57618
Montalukast.mol	-69.6583	31.97168	-0.23045	3.754623	19.91152
EGCG.mol	-68.4809	-47.7471	-4.51799	-0.60522	8.252421
epigallocatechin gallate.mol	-68.4809	-47.7471	-4.51799	-0.60522	8.252421
Calpain inhibitor II.mol	-67.6567	-14.9557	-1.67816	0.140831	16.83133
Tipranavir.mol	-67.6154	-33.4979	-5.47776	0.750869	19.98634
Montalukast.mol	-67.5512	20.74265	-0.42192	2.064023	29.02754
MK 0893.mol	-67.1466	28.36683	-2.304	0.492988	14.8435
MI-11.mol	-65.7389	-10.7837	-0.51179	0.581371	16.3482
paritaprevir.mol	-65.3896	5.337675	-2.17074	-1.22375	16.55192
Evans blue.mol	-65.219	31.72677	-3.43992	-0.01593	11.88529
Candesartan cilexetil.mol	-64.3248	-14.326	-0.24778	0.993928	7.154427
Lopinavir.mol	-63.971	-15.1333	0.081587	5.556572	22.50718
Calpain inhibitor XII.mol	-63.1818	1.958649	-0.10744	1.987974	23.21205
Adomeglivant.mol	-62.857	27.309	-0.86937	-0.00437	24.75256
Pimozide.mol	-62.6384	-24.9639	-1.26346	0.247478	3.741092
MI-05.mol	-62.5302	-14.3359	-1.14227	2.181828	24.84288
Calpain inhibitor I.mol	-60.2316	-15.9681	-2.30429	1.200495	8.575227
MI-09.mol	-60.147	-16.0875	0.442971	2.344829	14.14187
Z-FA-FMK.mol	-59.4649	-20.9182	-1.04617	2.397332	11.66063

gallocatechin gallate.mol	-59.2419	-28.7576	-2.94888	0.603376	16.63603
Hydroxychloroquine.mol	-58.8304	-16.9067	-0.7524	0.025967	18.71834
MI-13.mol	-58.2809	2.446406	0.597067	1.570739	11.11046
Vanitiolide.mol	-57.5212	-5.88571	-0.67403	0.020218	0.076975
Amentoflavone.mol	-56.9668	-20.1864	-1.17722	0.070948	19.48812
Rimonabant.mol	-56.7805	14.354	0.692432	0.406329	10.67064
Roxatidine acetate hydrochloride.mol	-54.7318	-13.623	-1.40166	-0.01156	16.26455
CAY-10581.mol	-54.1257	-6.46045	-1.98949	0.29425	18.39815
Baicalin.mol	-52.9559	-12.7537	-1.9767	0.205122	-0.36991
GC-376.mol	-52.5508	-6.78401	-1.77961	1.919932	20.90074
GC-376.mol	-52.5508	-6.78401	-1.77961	1.919932	20.90074
Oxiconazole.mol	-52.2478	8.612292	2.94407	1.230448	19.32063
Sertaconazole.mol	-52.1886	-10.8865	-0.36158	0.260188	9.842991
Trihexyphenidyl.mol	-52.0306	-10.5502	0.933398	-0.05322	19.53348
MI-21.mol	-51.9953	6.842978	-1.1322	0.234038	16.16411
MI-23.mol	-51.8745	-12.8773	-1.13253	5.596924	17.8447
ivermectin.mol	-51.4463	-6.35094	-0.78411	4.453476	17.082
Beta-sitosterol.mol	-51.3484	-9.61755	1.035676	0.884416	11.14183
Bepridil.mol	-51.1083	-13.1556	-1.14674	0.383959	4.970087
Clemastine.mol	-50.559	2.24233	0.070094	-1.54065	11.85841
sepantronium bromide.mol	-50.2317	-3.49499	-1.25093	0.061821	19.23059
MI-14.mol	-49.0974	-13.3611	-1.86301	-0.00645	21.24961
MK-886.mol	-49.0726	42.49613	-0.38318	0.30826	9.341153
Hexachlorophene.mol	-48.7088	2.142863	-0.04177	0.257609	13.64987
GSK-3965.mol	-48.7018	30.18991	-2.23196	2.020639	16.8589
dipyridamole.mol	-48.4389	-4.28109	-1.54562	0.252716	16.62875
MAC-30731.mol	-47.5416	-9.41454	0.551276	0.238235	11.29687
Chloroquine.mol	-47.4907	-7.37209	-0.11146	1.034253	9.469464
NSC 95397.mol	-47.1204	-16.8761	-2.22177	0.063106	12.93288
MG-149.mol	-46.6709	20.56752	0.10636	0.054866	12.88595
Sinigrin.mol	-46.1244	-22.294	-3.42828	0.045667	10.16121
Metixene.mol	-45.1158	-16.1847	-0.71031	0.605851	27.30188
Zopiclone.mol	-44.8612	-8.65357	2.378086	1.888059	22.50347
Tideglusib.mol	-44.3717	-19.738	-1.53915	0.711292	12.89542
Aloeemodin..mol	-43.7853	-14.0345	-1.85926	-0.02094	13.81896

Maribavir.mol	-42.8806	3.689906	-2.48415	0.094852	20.96531
SU 16f.mol	-41.9527	36.00816	-1.24758	-0.03526	16.85648
Fascaplysin.mol	-41.8435	6.384861	0.362245	-0.01228	25.51271
2,3,4-Trihydroxy-4â€™-ethoxybenzophenone.mol	-41.5183	1.474949	1.026868	0.069862	24.54076
Omeprazole.mol	-41.4537	-15.2709	-1.89712	0.098519	13.22828
3,4-Didesmethyl-5-deshydroxy-3â€™-ethoxyscleroin.mol	-41.2265	0.446117	-1.04302	-0.04325	21.73373
Disulfiram.mol	-40.865	-13.1748	0.585421	0.319478	7.680236
SP 100030.mol	-40.3066	17.78	-0.71519	0.025837	17.83289
Duloxetine.mol	-39.5556	-22.8317	-2.5315	0.673852	19.84109
beta-lapachone.mol	-39.1741	20.37711	-0.10227	0.016647	13.91587
Shikonin.mol	-38.8533	2.64161	0.444208	-0.02378	12.99708
Anacardic Acid.mol	-37.6581	18.16537	0.335896	0.102528	19.69273
GW5074.mol	-37.5183	12.39665	-0.49636	-0.00405	25.39252
Cimetidine.mol	-36.9758	-17.6513	-2.00223	0.02843	10.59787
AMG-837.mol	-36.6403	39.18907	0.412902	3.075795	24.29245
Baicalein.mol	-35.9868	3.605957	-0.65178	-0.00138	23.34554
walrycin B.mol	-35.9061	17.83741	1.122539	-0.01427	22.16037
Daidzein.mol	-35.7898	3.608061	0.431031	-0.00488	18.50123
Leteonin.mol	-35.3462	9.277312	-1.34122	0	24.54566
Hesperetin.mol	-35.2997	7.881633	-1.05896	-0.00549	13.57944
Oxytetracycline.mol	-32.4105	-1.35685	-1.60355	-0.06807	8.338147
Plumbagin.mol	-32.0953	-14.0399	-1.46724	-0.00104	16.36426
PX-12.mol	-28.5036	-13.7177	-1.00984	-0.14028	5.705598
Carmofur.mol	-26.6082	5.983489	1.999898	0.04204	14.93048
Theaflavin.mol	-26.4437	-2.70997	0.032061	-0.00177	17.27129
MAC-22272.mol	-26.3336	-2.8099	-0.54048	-0.00022	15.96191
Valacyclovir hydrochloride.mol	-26.1219	1.782789	0.125651	0.08974	28.36763
agaric acid.mol	-23.4954	90.31782	-1.73438	-0.04728	12.60234
Chloranil.mol	-23.0971	-9.14319	-1.08183	-0.00151	17.89613
LLL-12.mol	-22.13	-2.4805	-1.47439	-0.06814	19.585
untitled.mol	-20.5154	16.18468	0.718214	0.130406	9.259403
Sulfacetamide.mol	-20.4126	16.60043	-0.02403	-0.00468	21.11088
Thimerosal .mol	-20.3094	22.45001	-0.65201	0	9.642237
Rottlerin.mol	-20.1277	-28.7002	0.361376	0.197384	16.43543

Bronopol.mol	-16.8182	-17.0048	-2.4621	0	14.70356
Quercetin,.mol	-16.641	-25.7137	-2.2295	-8.37E-05	21.52464
MAC-13985.mol	-15.9207	-23.3309	0.458516	0	1.657278
Indican.mol	-11.0471	34.08022	-0.25148	6.09E-05	17.3763
Indirubin.mol	-9.30218	-6.01018	0.216765	-0.00134	22.86862
DA-3003â˘’1.mol	-6.47423	29.63612	0.132727	0.081064	23.15773

2.5 Molecular dynamics simulation (100 ns)

Utilizing programs and the OPLS3 force field, MD modeling of the additional reliability docked 107/6XQS compound was carried out in order to better confirm the outcomes of 3D- QSAR and molecular docking. TIP4P moisture was used to solvate the molecular structure in an orthorhombic box while maintaining a minimum spacing of 10 between the solution and every face of the box[23]. The solvated complex has a final box volume of 286,783 3, 2842 protein atoms, 1428 weighty atoms, and 10030 water particles. Up until a gradient threshold of 25 kcal/mol/ was met, the solvated complex was exposed to LBFGS reduction with 3 vectors and a least of 10 steepest decline stages. 2000 iterations in total were made during reduction, with a converged criterion of 1.0 kcal/mol/. The reduced structure was then progressively warmed to 300 K at 1 bar of temperature with a 2-fs time step in the NPT array. The Nose-Hoover regulator controlled the heat and air, correspondingly[24]. With a tolerance of 1e-09, the particle mesh Ewald technique was used to handle long-range electrostatic connections, while a cutoff size of 9 was used for short-range non-bonded conversations. After that, the reduced network was modeled for 30 ns, with data being taken every 100 ns during the MD run. For simulations of bonded, near non-bonded, and distant non-bonded contacts with time steps of 2, 2, and 6 fs, correspondingly, the multiple time step RESPA integrating technique was utilized. The Maestro graphical user interface was used to analyze trajectory and three-dimensional formations.

3. Result and discussion

3.1 Pharmacophore simulation and 3D-QSAR investigations

Eight of the most potent compounds were used to create a pharmacophore model of GyrB regulators. Two hydrogen bond acceptors (A), one hydrophobic (D), one hydrogen bond donor (H), and one aromatic ring (R) make up the best five feature model AADHR.187 (Fig. 1a,b). In the series of data sets chosen, these five characteristics were discovered to be crucial for the MPro inhibitory action[25]. The alignment of hypothesis AADHR.187 over active (pIC50 6.20, Fig. 1c) and inactive (pIC50 4.57, Fig. 1d) molecules shows that the intervening site distances account for the majority of the difference between active and inactive agents. With low power (0.339) and inactivity, this model had the greatest survival (3.263), gradient (1.156), site (0.71), vector (0.913), and volume (0.643) scores (1.107).

The trained set substances' scientifically significant ratio of findings (R2 = 0.986 in Table 2) and testing group compounds' scientifically relevant coefficient of determinations (R2 = 0.986) revealed a good agreement between the anticipated and actual IC50 activity levels. The strong cross verified correlation coefficient (Q2 = 0.798) for the testing set chemicals at four PLS is responsible for the model's excellent level of predictability and dependability. Also, a larger variance ratio (F = 417.36), Pearson-r of 0.894, stability of the model (0.779 on a scale of 1), and a lower P value (8.44e-23) showed a higher level of trust in the approach. Additional evidence that the data utilized for model building is the optimum for QSAR analysis comes from decreased values of the SD = 0.120 and RMSE = 0.210 Table 1.

Figures 2a and 2b, correspondingly, illustrate the connection between practical performance and Phase (v4.6) projected operation of the training and testing sets. The scatter plots of the trained and testing sets show that there are some modest discrepancies between the exploratory and phase anticipated performance[26]. By forecasting the action of the ten external testing set elements E1-E10, the statistically robustness and usefulness of the best developed model AADHR.187 were confirmed. The findings are shown in supplemental Table S4. The data vs. projected pIC50 plot of the exterior test set shows that the system was capable of sustaining the real pIC50 values for the substances. A baseline plot is created, which is utilized to identify outliers in a QSAR[27]. The residue plot makes it clear that this research does not include an outlier. Thus, the created model AADHR.187 is regarded as stable. A forecast correlations factor (R2) value of 0.65 was found for the external testing sample for the QSAR modeling that was constructed, and as a result, the model is thought to be able to forecast the MPro inhibiting ability of compounds that were not incorporated in the modeling construction[28].

The model found all of the active compounds in the target list. To assess the effectiveness of the created model in differentiating actives from inactives, the enriched features (EF) and robust initial improvement (RIE) were determined[29]. The ranking of the finest suited model, AADHR.187, was found to be better than the random distributed with a RIE value of 8.65 and a BEDROC value of 1.00. Also, the AUC of the ROC curve was used to assess the system's efficiency. The current algorithm exhibited excellent AUC (1.01) and ROC (0.96) values Table 3.

3.2. QSAR research using outline plots (short)

To comprehend the impact of the spatial configuration of physical elements on their MPro inhibitory action, QSAR contour plots were examined. The red cubes denote undesirable properties, whereas the blue cubes by default represent positive qualities that contribute to the ligand contacts with the targeted enzyme. The simulation was used to evaluate the most important beneficial and detrimental locations for hydrogen bond donor, hydrophilic, and electron absorbing units in the highly active molecule 107 (pIC50 = 7.854) and the lesser active molecules 1 and 29. (Fig. 3a-f) [30,31]. The decreased activity of compound 1 (Fig. MPro) and additional compounds from the pyridylurea (2-16) (pIC50 4.161-6.026) and triazolo[1,5-a] pyridine (pIC50 3.834-4.985) series, which lack an NH group in their respective pyridyl and triazolo[1,5-a]pyridine rings, correspondingly, confirm this hypothesis. A favoring of hydrogen bond donating units at this location for MPro inhibitory action was shown by the development of blue cubes at location three of the pyridyl ring[32], which is present at point seven of the benzimidazole scaffold. Additional evidence that the hydrogen bond donor band at this location is undesirable for the activity comes from the development of red cubes surrounding the carbonyl oxygen of the ethyl urea moiety[33].

The activity is also significantly impacted by the hydrophobic nature of the element. The presence of blue squares around the ethyl fragment of the ethylurea moiety and a portion of the imidazole ring in the most active component 107 (Fig. 3c) demonstrated the selectivity of hydrophobic groups at these sites[34]. The presence of blue cubes around the pyridyl rings at locations three and four of the pyridyl ring located at position five of the imidazole scaffold, as well as at position seven of the imidazole ring, suggested the predilection of hydrophobic compounds at these places. Red cubes that appeared at the benzimidazole's ring junction showed that an electron-withdrawing unit did not choose to occupy this place[35–38]. Red cubes emerged in the contour map of another low-activity compound 1 around the nitrogen of the pyridyl ring linked to the ethylurea moiety and around the carbonyl unit of the ethylurea moiety (Fig. 3f), indicating that electron absorbing units do not favor these sites.

3.3. Molecular docking

The chosen inhibitors 1-107 were subjected to extra-precision docking computations in this work to forecast probable binding conformations. With a root mean square deviation (RMSD) of 0.956, the co-crystal ligand's extra-precision docking posture was comparable to its testable decided configuration (pdb.6XQS), as displayed in Fig.5, demonstrating the high consistency of docking protocols in generating the binding mode of chosen inhibitors 1-38. Because of the presence of an ATP-binding active center in that area, contacts with the majority of the active inhibitors were mostly seen in the range Ser43 to Thr163. The side chains of the polar and charged acids Asn42, Ser43, Asp69, Arg72, Arg132, and Thr163 surround the majority of the active inhibitors in a hydrophilic pocket that is conducive to hydrogen bonds and ionic contacts (Fig. 4a-d). The electrical and van der Waals energy elements of the force field OPLS3 are heavily weighted, and strong negative values of Emodel [39,40] showed that hydrogen bonds and ionic interactions are the main drivers, with hydrophobic contacts providing a small contribution.

Compounds 1, 29, 34, and 36 were chosen as a point of reference for in-depth examinations of their 6XQS binding mechanisms. In instance, the two NH groups of the ethylurea moiety of 1, 29, 34, and 36 displayed hydrogen bonding contacts with the backbone carboxylate oxygen of Asp69, a crucial binding site of the ATP catalytic region, in a bidentate manner [41]. As a result, the inhibitor's hydrogen bonding interactions with 6XQS depend on these two NH groups. The development of blue cubes surrounding the NH groups of the ethyl urea molecule in the contoured plot study further revealed the importance of these parties for hydrogen bonding connections. The backbone OH of Ser43 created an extra hydrogen bond with the NH of the -NHC2H5 segment in the least active molecule 1 (NHOH, 2.2). In the case of this molecule, the triazolo[1,5-a] pyridine scaffold's position six pyridyl ring and the NH2 of Arg72 showed a -cation connection (Fig. 4a). While the nitrogen of the pyridyl ring located at position six of the triazolo[1,5-a] pyridine scaffold accepted a hydrogen bond from the spine NH of Arg132 (rNNH, 2.5) in a further low active ingredient 29, N1 of the triazolo [1,5-a] pyridine ring founded a hydrogen bond with the spine OH of Thr163 (rNHO, 2.5). (Fig. 4b). Similar to compound 1, this pyridyl ring had a -cation connection with Arg72's NH2.

The highest active molecule 34 had five hydrogen bonds, two more than the least active ingredient 1[42]. In molecule 34, both NH of the ethylurea moiety developed bonding relationship one every with carboxylate oxygen of Asp69. This molecule also displayed hydrogen bond formation, one each with Asn42, Arg132 and Asn42. The N3 of the benzimidazole ring acquired a hydrogen bond from the core NH of Thr163 (rN···HO, 2.0 Å), whereas NH of the same ring created a hydrogen bond with carbonyl oxygen of Asn42 (rNH···O=C<, 1.99 Å). Similarly compound 29, the nitrogen of pyridyl ring located at position six of the triazolo[1,5-a]pyridine scaffold likewise displayed a hydrogen bonding contact with the backbone NH2 of Arg132 (rN···HN(H), 2.0 Å) (Fig. 4c) (Fig. 4c). Nevertheless, no π-cation connection was detected in compound [41]. Like 34, molecule 36 also displayed three hydrogen binding contacts, two with Asp69 ((O=C)NH···¯O-C=O, 1.8 Å and -C2H5NH···¯O-C=O, 1.9 Å) and one with Arg132 (rN···HN(H), 2.3 Å). A π-cation connection with Arg72 was also detected (Fig. 4d) for this molecule (Ren et al., 2022). Additionally, comparable to the highly active compound 34, compounds 1 and 29 includes less hydrophilic end, leading in a lower hydrophilic space-filling in the binding pocket. Perhaps this might be the cause for the reduced binding selectivity and effectiveness of compounds 1 and 29.

3.4 Binding free power estimation

The binding free energy of 1-107/6XQS compounds was calculated using the structural “mechanics-generalized born space area (MM-GBSA)” method in order to assess the extra-precision docking. The MM-GBSA is a data preprocessing end-state approach for precise classification of ligands depending on the free forces of binding that is significantly more effective. In the current study, there was only a weak connection (R2 = 0.294) between the measured IC50 values and the predicted free energy of binding (Gbind). The computed Gbind has a range of -24.128 to -65.546 kcal/mol, with the van der Waals (GvdW) and non-polar solvation (GLipo) energy components for inhibitor binding making up the majority of the value. On the contrary, in majority of the active inhibitors the electrostatic interface (ΔGCoul) marginally favor, while electrostatic solvation (ΔGsolv) energy phrase firmly the binding to the MPro enzyme. The fact that covalent energy (Gcov) term somewhat inhibits inhibitor binding in the majority of active inhibitors is also clear from the results. Also, the fact that GvdW is substantially stronger than GCou and GLipo suggests that van der Waals interactions is what really causes the inhibitor to attach to the MPro enzyme in SARS-CoV-2. This is in line with past research [43–45] and the results of extraprecision docking, where the

GvdW energy term also substantially favors inhibitor binding. The energy efforts from the high active substances 34, 36, and 37 were considerably greater than those from the least active molecule 29 (GvdW -40.94 kcal/mol; GCoul -32.30 kcal/mol) in terms of GvdW (-62.70, -58.56, and -61.74 kcal/mol, correspondingly) and GCoul (-51.00, -44.51, and -40.13 kcal/mol.

3.5 Molecular modeling computation Molecular dynamics study

Desmond software program (v4.5) was used to do an MD model in aqueous phase to check at the durability of the enzyme combination. Using the MD model to evaluate the structural prerequisites for the inhibitory action, the docking-simulated designed modeling of the 38/6XQS combination was employed as the starting configuration. To investigate the dynamic durability of the solution, the “root mean square deviations (RMSDs)” for the backbone, C-, and heavy atoms of protein were examined. Fig. 5a shows the RMSDs of the network during MD simulation in relation to its initial configuration. The figure clearly shows that the unit is in a balanced structure during the course of the 100 ns MD experiment. Over the first 13.5 ns of the path, the RMSD of the complex core, C-, and heavy atoms climbed to 1.86, 1.84, and 2.16, correspondingly, before becoming stable (in the range 1.11-11.25, 1.09-1.21, and 1.46-1.63, respectively) in the latter portion of the simulation. The inclination of the binding pocket residues' RMSD to accommodate ligand movement is seen in Fig. 5a. The radius of gyration (rGyr) for each backbone (red triangle) and C-atom (blue circle) atom was calculated as a result of the MD simulation duration in order to further investigate the protein's durability. The rGyr of the 38/6XQS complex's foundation and C-atoms steadily increased (16 and 16.02, respectively) up until 7 ns before stabilizing in the ranges of 15.84-16.03 and 15.76-16.05, respectively. This indicates that the virtual scheme is in a comfortable configuration as a consequence of the solvent influence [46–50]

In addition, the root mean square fluctuation (RMSF) of the protein's spine and C-atoms in the 38/6XQS combination was investigated. The area Glu81-Glu82, which is found on loop Asp70-Ala86 linking -sheet (Leu65- Asp69) and -helix, is where the residues with the highest flexibilities are distributed, according to the backbone, C-α, and heavy atom RMSF values measured (Fig. 5b) (Val87-Cys92). These three residues' RMSF values are compatible with the B-factor, which is measured to be between 46.36 and 51.35 2. We contrasted the B-factor from the all-atom MD computation with the average B-factor from the crystal structure (6XQS.pdb) to confirm the converging of the dynamic assignment of the system. The B-factor for the MD modeling was in the range of 14.33 to 23.95 2, which is close to the average B-factor for protein crystal structures (25 2) and indicates that the residues in catalytic pockets are rather stable. Although no interactions were seen in the flexible areas Ala47-Glu66 and Asp133-Gly162, ligand-protein contacts were seen in the regions Val39-Glu46, Val67-Pro75, Ile90-Arg132, and Thr163-Val165.

We contrasted the binding posture of the average organization of 34 during MD modeling with the XP-Glide docking position to better examine the receptor-ligand relationships (Fig. 4c). All five of the hydrogen bonds found in the XP-docking are maintained for 13–100% of the MD path (Fig. 5c). Both of the NH groups of the ethyl urea moiety made strong hydrogen bonds with the Asp69 side chain carboxylate oxygen atom in the MD modeled107/6XQS complex, forming 100% of the MD path in both cases. In addition, Asp69 also received a medium frequency hydrogen bond from the nitrogen at location three of the benzimidazole ring (26% of the MD path). Moreover, the benzimidazole ring's nitrogen atom demonstrated weak hydrogen bonding networks with the residues Gly73 and Thr163 (24 and 13% of the MD trajectory, respectively). Since Asp69 has limited structural flexibility, as seen by its low dihedral angle (∈ = 43°) and high B-factor (16.30 2), there are strong hydrogen bonding systems with this position. A straight bond (51% of the MD trajectory) and a crossbridged bond (20% of the MD trajectory) were created by the nitrogen atom of the pyridyl ring located at location five of the benzimidazole ring with the side chain of Arg132. A strong salt bridge contact between this nitrogen atom and Arg72 (18% of the MD trajectory) was also produced. Moreover, a weak -cation contact with Arg72 was established by the position five pyridyl rings (22% of the MD path). The considerable conformational versatility of this residue (∈ = 342°) caused by the dynamic body motion of the -helix residues Cys92-Val87 is the cause of these weak hydrogen bonding contacts with Arg72. The side chain of Asn42 (which makes up 50% of the MD trajectory) and the carbonyl oxygen atom of the ethyl urea moiety were shown to interact strongly via hydrogen bonds. The decreased conformational versatility of Asn42 and Arg132, which are reported to have strong hydrogen bonding interactions (∈ = 57° and 58°; B-factor 18.27 and 26.21 2, accordingly), is the cause of this. The data shown above clearly show that the stability of the inhibitor inside the catalytic pocket is mostly owing to hydrogen bonding contacts with the important binding residues Asn42, Asp69, and Arg172, with hydrophobic contacts only having a minimal impact. This is consistent with past research (Bellon et al., 2004; Charifson et al., 2008), as well as large negative values of GCou and GvdW computed using the MMGBSA technique (Asproni and Gessi 2023).

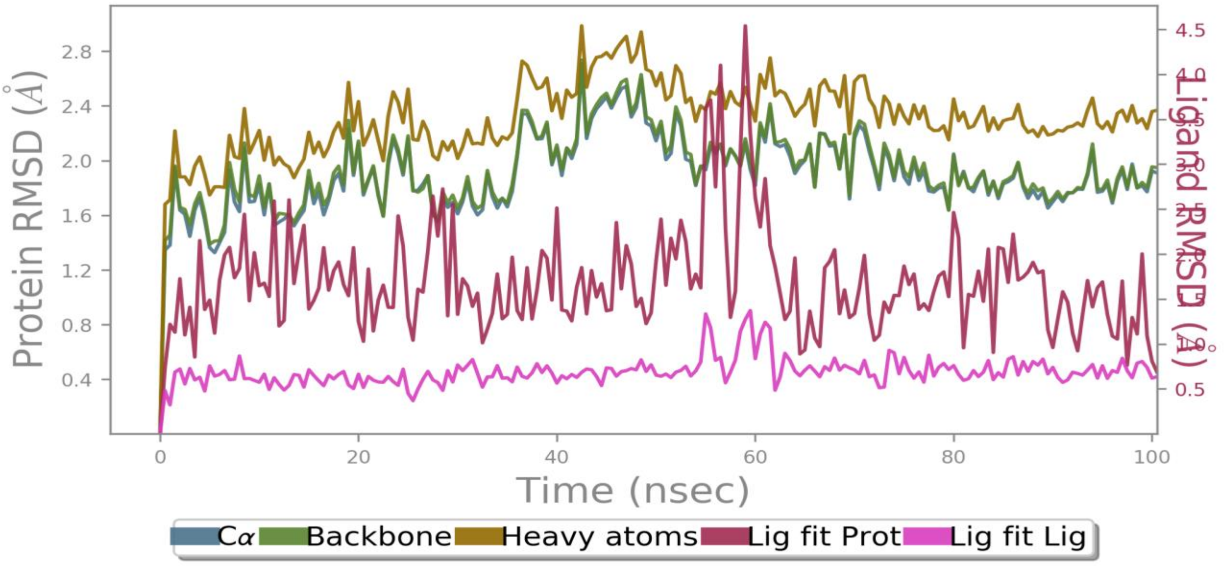

(a)

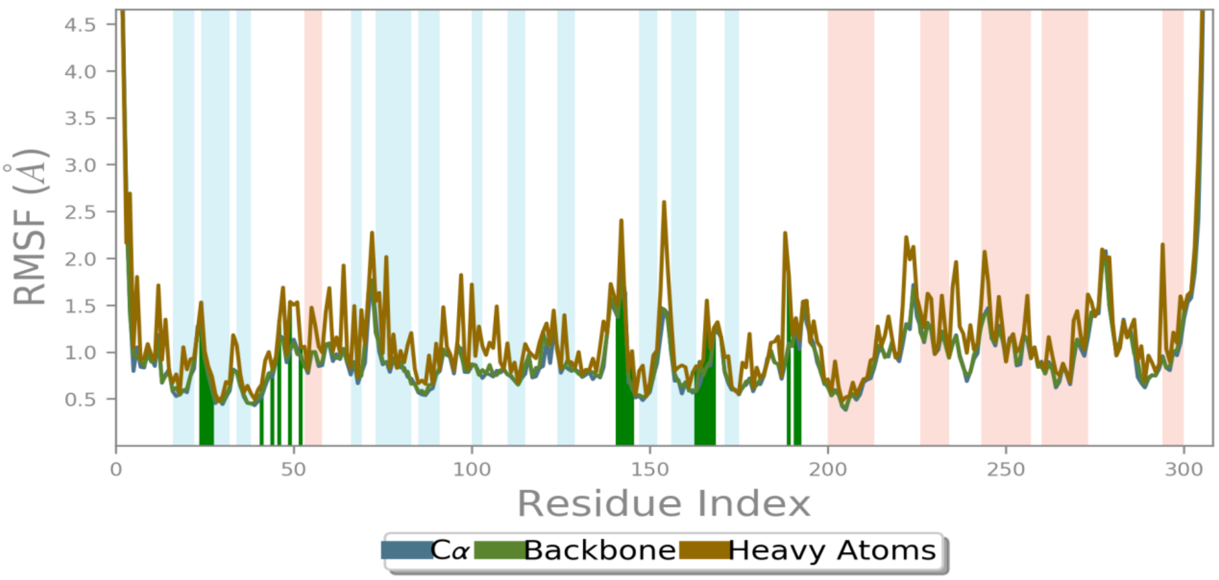

(b)

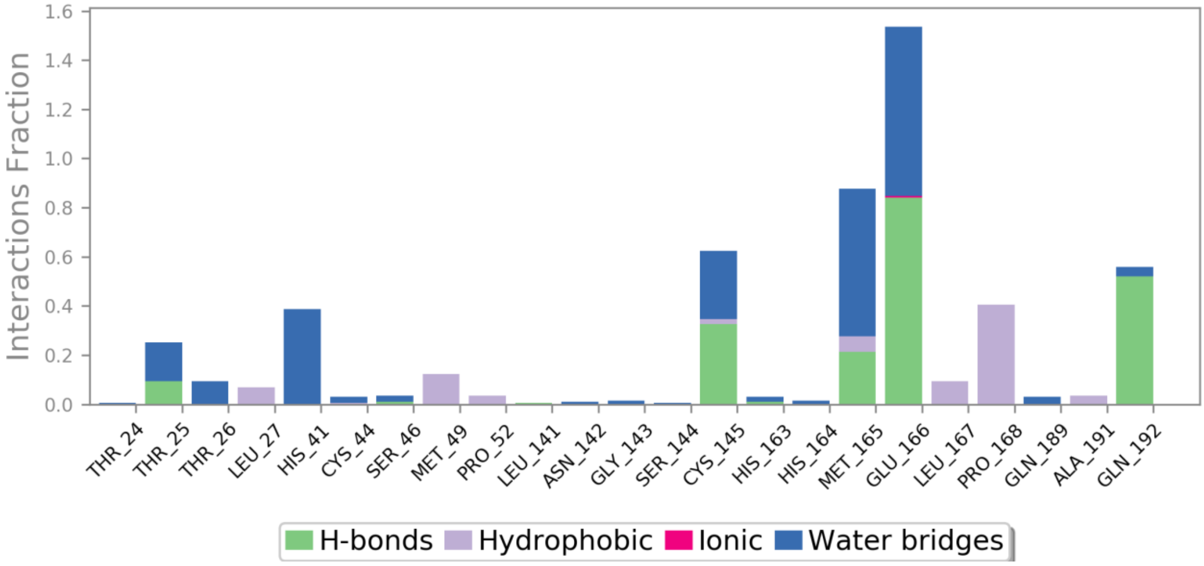

(c)

Fig. 7. Plots show MI06 (a) RMSD profile of the C- and spine atoms of the 38/6XQS complex, (b) the RMSF profile of the 6XQS catalytic pocket residue, and (c) the association of inhibitor 107 with the catalytic pocket residues of 6XQS during the 100 ns MD modeling.

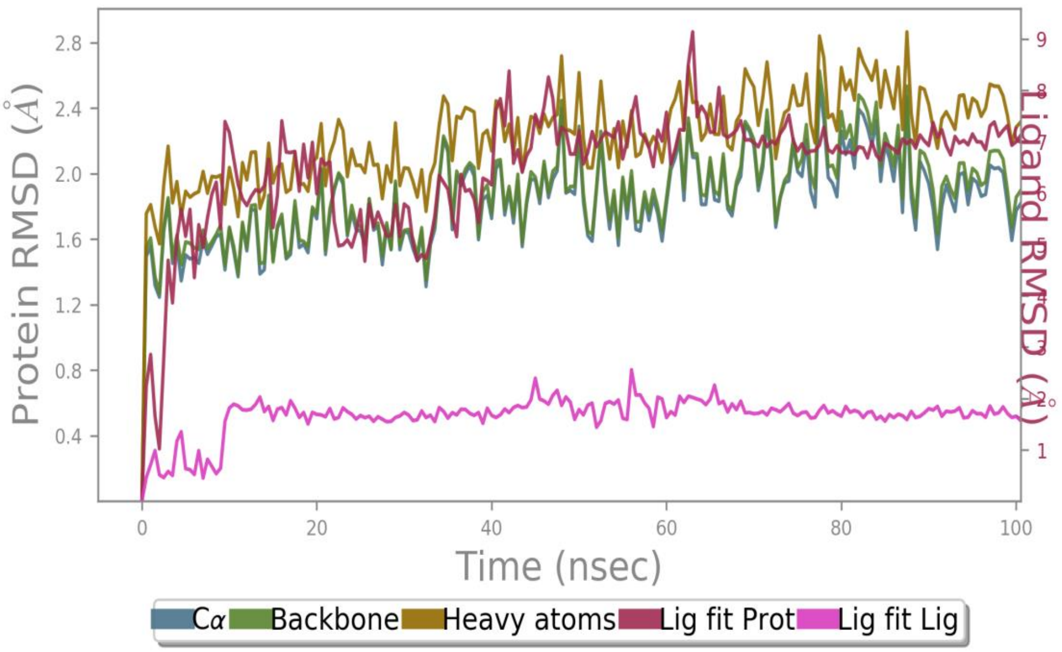
Protein RMSD (Å)
2.8
2.4
2.0
1.6
1.2
0.8
0.4
Ligand RMSD (Å)
9
1
0
20
40
60
80
100
Time (nsec)
Cα
Backbone
Heavy atoms
Lig fit Prot
Lig fit Lig

(a)

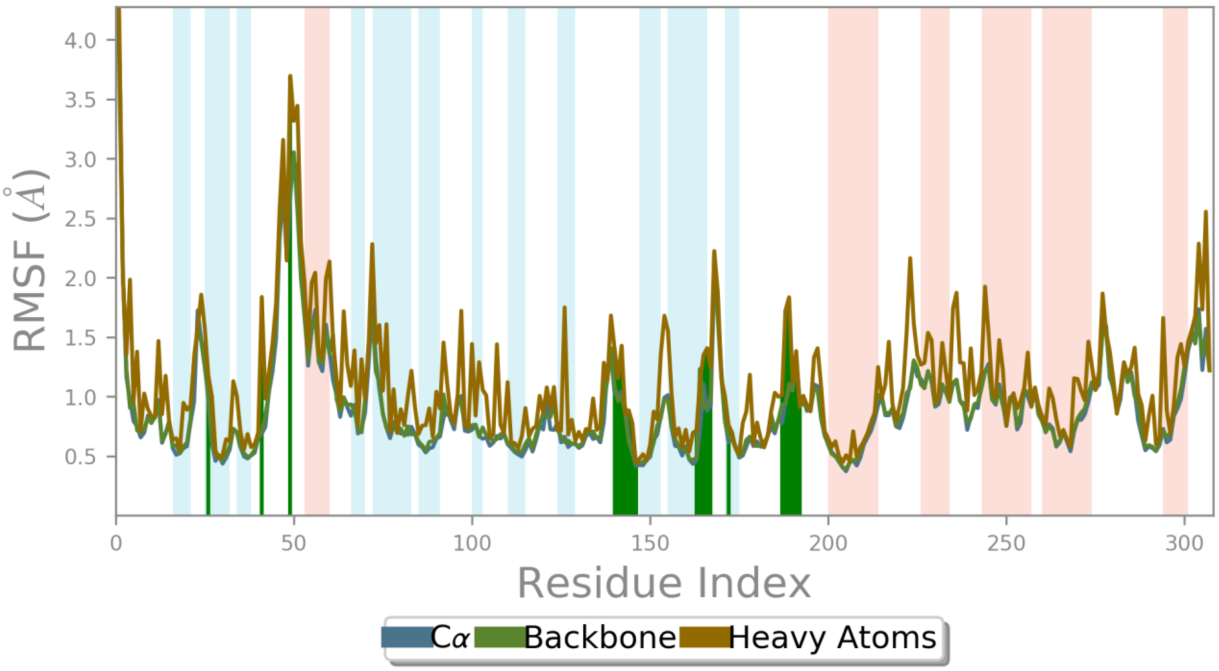
RMSF (Å)
4.0
3.5
3.0
2.5
2.0
1.5
1.0
0.5
0
50
100
150
200
250
300
Residue Index
Cα
Backbone
Heavy Atoms

(b)

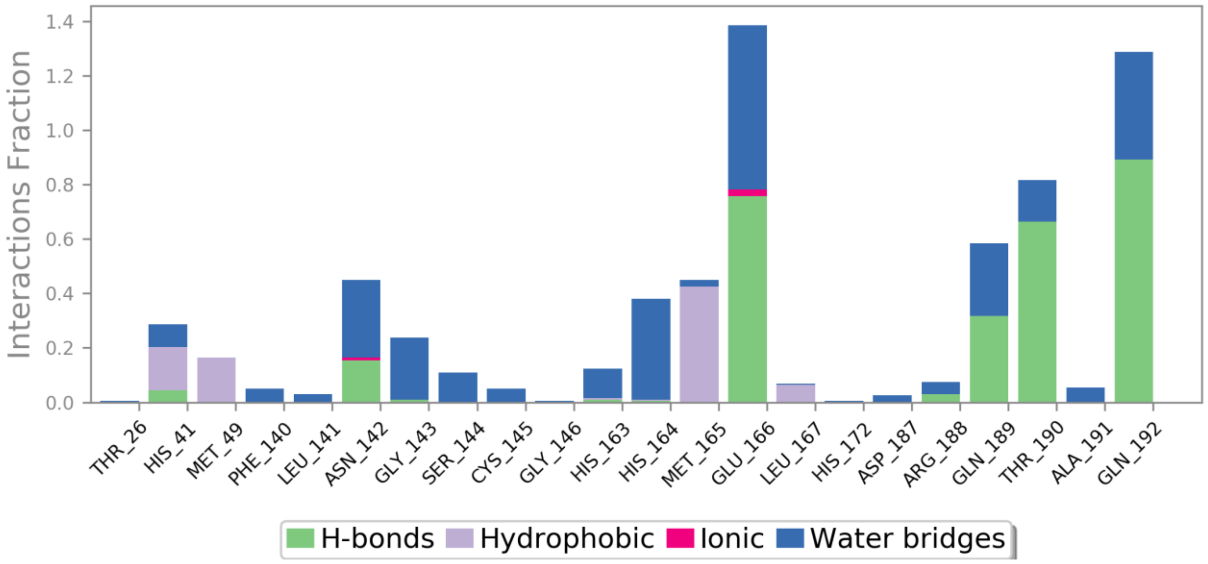

(c)

Fig. 8. Plots show Baicalin (a) RMSD profile of the C- and spine atoms of the 38/6XQS complex, (b) the RMSF profile of the 6XQS catalytic pocket residue, and (c) the association of inhibitor 107 with the catalytic pocket residues of 6XQS during the 100 ns MD modeling.

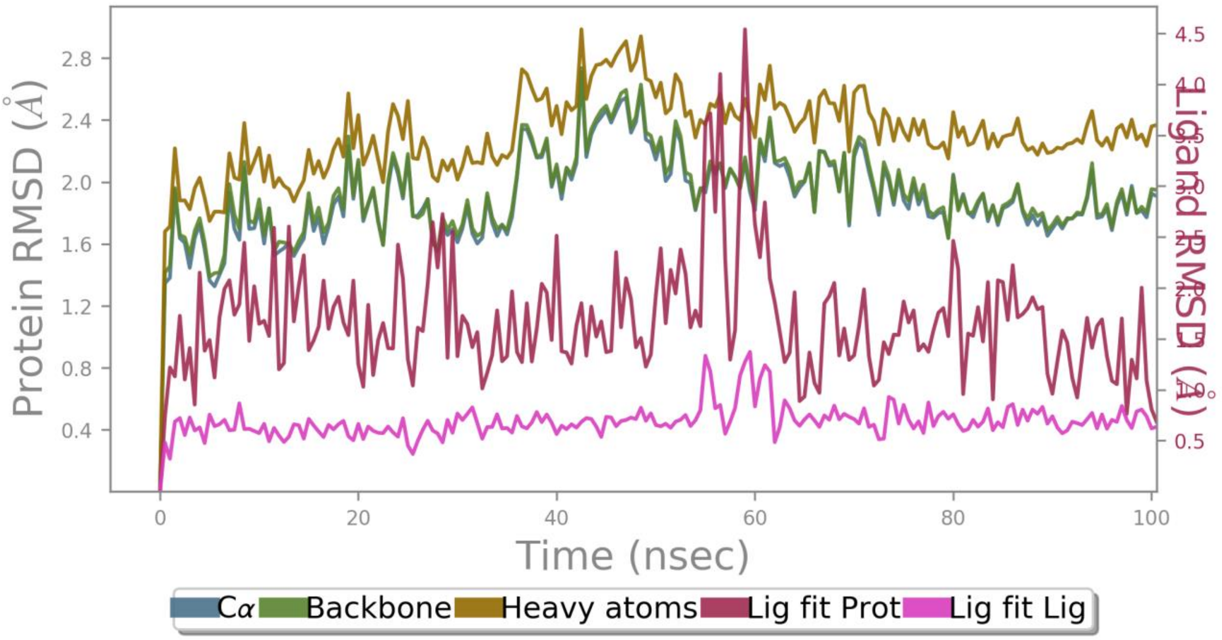

(a)

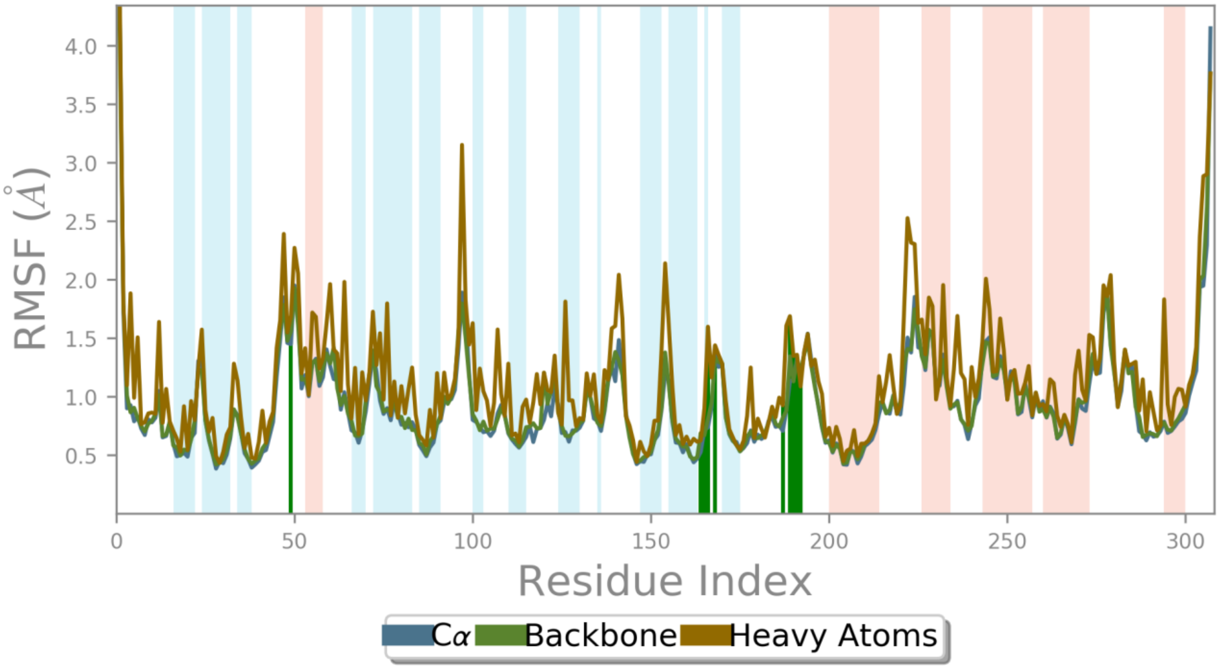

(b)

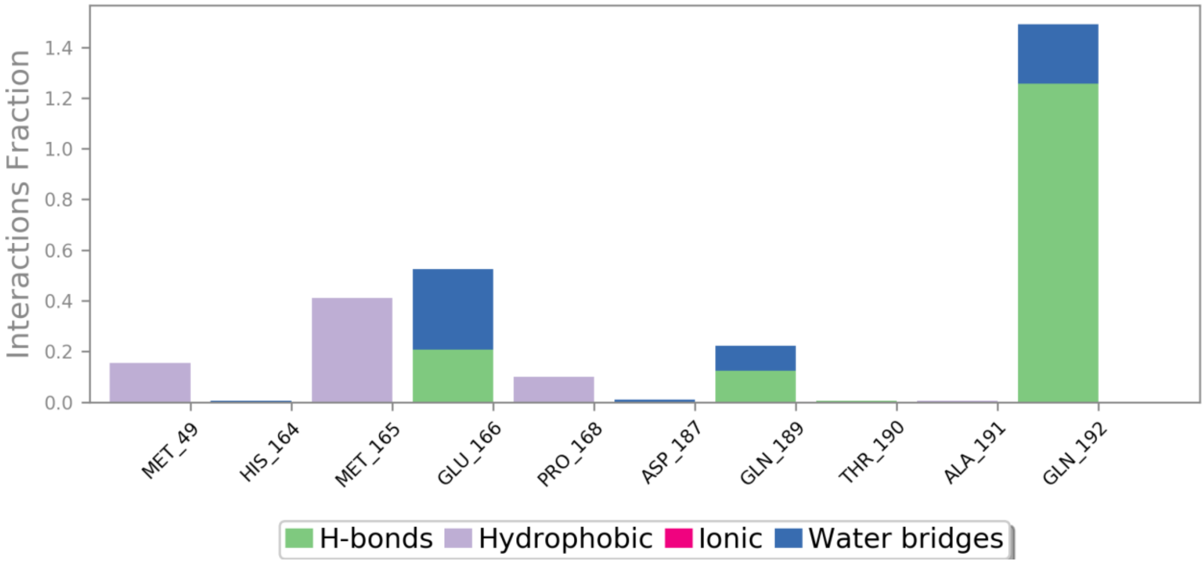

(c)

Fig. 9. Plots show Benzophenone (a) RMSD profile of the C- and spine atoms of the 38/6XQS complex, (b) the RMSF profile of the 6XQS catalytic pocket residue, and (c) the association of inhibitor 107 with the catalytic pocket residues of 6XQS during the 100 ns MD modeling.

Also, after 3 ns of MD simulation, inhibitor 107 had a radius of gyration (rGyr) and RMSD in the ranges of 4.42 to 4.55 and 0.27 to 1.26, respectively. This suggests that the inhibitor will behave more predictably and steadily throughout modeling. Moreover, polar surface area (PSA) (202.56-232.43 2) and a stable solvent exposed surface area (SASA) (35.19-124.72 2) were seen from 2 ns to 30 ns (100.57-190.45 2), showing the stability of ligand inside the catalytic pocket [49]. Minimal fluctuations in the inhibitor's polar surface area (117.55-142.42 2) and molecular surface area (342.49-350.97 2) further enhanced the stability of the inhibitor inside the catalytic pocket throughout the 30 ns MD path. The solvent exposed surface area (SASA) was found to be between 139.77 and 180.75 2 during the final 10 ns, suggesting that the majority of the inhibitor 107 was buried within the catalytic region. The variants of 107 best XP-docking position and the posture of the AADHR.187 system, as well as the crystal structures of 34 after MD modeling and the pose of the AADHR.187 prototype, showed high agreement (RMSD: 1.35, 1.42, and 1.17 respectively.

3.6. High-throughput in silico virtual scanning (HTVS)

Using the Schrödinger Suite 2020-1, we carried out high-throughput digital testing focused on pharmacophores. The finest generated pharmacophore hypothesis AADHR.187 was used as 3D searching questions with the roughly 1,550,000 chemicals in the collection datasets (Khetan (2023)). Chemically similar molecules that have excellent spatial overlap with the related pharmacophoric modeling AADHR.187 characteristics were identified as hits [43,44]. The acquired virtual hits were put through Glide SP (standard precision) docking, and 50 of the highest-scoring virtual hits were chosen depending on Glide score, hydrogen bonding, and hydrophobic contacts in the catalytic region. Five compounds with a high selectivity for the binding region were chosen, and the binding free values of those molecules were determined using the Prime (v4.3) method and the MM-GBSA methodology[46]. The five top-ranked compounds' chemical structures are shown in Fig. 6, and the findings of digital scanning, XP-docking, and free binding energy calculations. Their top five virtual hits had positive Glide scores (-4.64 to -5.20 kcal/mol), binding free energies (-57.95 to -67.03 kcal/mol), hydrogen bonding associations with the important binding amino acid residues Asn42, Asp69, Arg72, Gly73 and Arg132, and -cation association with Arg72. All five of these results were found inside the protein's active area shell.

3.7. Insights into Design of New Mpro Inhibitors with Higher binding Affinity

The relevance of the 2-benzimidazoleurea scaffold was shown by examination of the produced contour plots, and this was supported by the extra-precision chemical docked and the 100-ns MD research with the MPro protein. We chose the most effective inhibitor, 107, as a model for the complexation of novel MPro inhibitors. The NH of the ethyl urea moiety and location one of the benzimidazole ring are both essential hydrogen bond donor parties, as is seen from the contour plot of hydrogen bond donor unit. The hydrophobic collective's preference for the ethyl fragment (H9 phamacophoric feature) of the ethyl urea moiety, the pyridyl ring at location seven of the imidazole ring, and locations three and four of the pyridyl ring at location five of the imidazole ring were further demonstrated by the contour plot of the hydrophobic group. We used bulky hydrophobic substituents on various places of both pyridyl rings located at locations five and seven of the benzimidazole ring depending on the results from the created 3D-QSAR model. In order to limit the single bond rotation of the -NH-CH2(CH3) moiety, we additionally replaced a large hydrophobic group on the pharmacophoric characteristic H9. In an effort to increase performance, we also attempted hydrogen bond donor units at locations three on the benzimidazole ring and three on the pyridyl ring at location seven on the benzimidazole ring [48].

We used electron withdrawing sections at locations three and four of the pyridyl ring available at role seven of the benzimidazole ring and also at location four of the pyridyl ring observed at location five of the benzimidazole ring centered on the binding pocket assessment and contour map of electron withdrawing categories (Fig. 3e). To further limit single bond rotation around the benzo portion of the benzimidazole and pyridyl rings, we used a variety of heterocyclic rings in lieu of the pyridyl rings found at positions five and seven of the benzimidazole ring (-C6H4-C-pyridyl). When tested against the top fitting 3D-QSAR model AADHR.187, chemical changes to inhibitor 34's benzimidazole urea framework significantly increased the projected efficacy. Fig. 7 depicts the three MPro inhibitors D1–D3 that were created based on the inhibitor 34's benzimidazole urea scaffold. The extra-precision chemical docking and binding free energy estimations are also applied to these developed inhibitors. The gliding scores and binding free energies of all three of the proposed compounds were favorable (ranging from -5.11 to -5.88 kcal/mol). These inhibitors displayed hydrogen bonding associations with Asn42, Asp69, Ile116, Gly73, and Thr163, important residues, and they fit well into the protein's activation site shell [51].

In the proposed compounds D1 to D3, the ethylurea moiety's two NH atoms displayed bidentate hydrogen bonding contacts with Asp69's backbone carboxylate oxygen. In molecule D2, the backbone carbonyl oxygen of Asn42 and the backbone NH of Ile116 each made hydrogen bonds with one NH and carbonyl oxygen atom of the ethyl urea moiety. With the backbone carbonyl oxygen atom of Asn42 and the carboxylate oxygen atom of Asp45, correspondingly, the hydroxyl hydrogen atom in compound D1 and the hydrogen atom of the carboxylic group in drug D3 displayed hydrogen bonding contacts. One nitrogen atom of the pyrazine ring and the NH of Arg132 formed an extra hydrogen bond in molecule D1. The extra-precision docking on drug D3 also revealed -cation contacts between Arg72 and the benzo portion of the benzimidazole ring.

The calculated binding free energies (Gbinds) of the proposed molecules D1-D3 and 6XQS complexes vary from -72.09 to -81.42 kcal/mol. The van der Waals (GvdW -52.65 to -60.03 kcal/mol) energy term substantially promotes the binding of designed molecules D1-D3 with MPro enzyme, as is seen from the binding free energy parts of compounds. The binding of D1-D3 is similarly favorably affected by the Coulomb energy term (GCoul -25.92 to -46.35 kcal/mol), but the covalent energy term (Gcov 4.84 to 9.71 kcal/mol) only marginally affects the binding. Also, it is shown that the non-polar solvation impact (GLipo -20.91 to -22.80 kcal/mol) is fairly beneficial for the binding in all three of the proposed compounds. The electrostatic solvation energy (Gsolv 23.84 and 41.58 kcal/mol, accordingly) term in compounds D1–D3 clearly favors dissociation over binding. Van der Waals forces are obviously what drives the binding of selected molecules D1-D3 to the MPro enzyme, as seen by the large negative levels of GvdW. These outcomes concur with the docking outcome. Also, the QikProp was used to predict the ADMET (absorption, distribution, metabolism, and excretion) characteristics of designed compounds D1-D3 (Schrödinger 2020-1). The developed compounds D1–D3 adhered to Lipinski's rule of five (0–2), demonstrating their drug-like characteristics. D1-D3's anticipated central nervous system (CNS) function was determined to be 2.0 on a scale of -2 as inactive, suggesting that there is no CNS function in these proteins. The range of 103.64 to 150.92 2 for Polar Surface Area (PSA), which is connected to the Van der Waals surface area of polar nitrogen and oxygen atoms, is well within the advised range of 7-200 A2. The calculated hydrophobicity of the molecule, QPlogPo/w, was found to be between 2.10 to 6.04, which is likewise within the advised range of -2.0 to 6.5. The expected apparent Caco-2 cell permeability, which serves as a model for the gut-blood barrier, was 124.14 nm/sec for D1 and 247.59 nm/sec for D2, respectively, showing that these molecules were not actively being transported. Although D3's lower Caco-2 cell permeability score of 9.31 indicates that this molecule is being actively transported. On a scale of 0 to 100%, the predicted human oral absorption of D1-D4 is between 67.53 and 80.59%. The projected IC50 values for developed compounds D1–D3 (QPlogHERG) for blocking HERG K+ channels vary between -3.59 and -4.34, confirming the security of these compounds. Moreover, compared to a suggested range of 300-1000 2, the solution accessibility surface area (SASA) varied from 617.6 to 907.23 2 [42].

4. Conclusion

To understand the structural foundation and inhibition process of 107 compounds active against the SARS-CoV-2 inhibitors, we adopted a combination analytical method in the current work. Utilizing 91 training and 16 testing dataset of molecules, we created the five-point 3D system AADHR.187, which is accurate. The developed modeling has a low RMSE (0.210) and SD (0.120), as well as a high coefficient of prediction (R2 = 0.986) and cross validation factor (Q2 = 0.798). The foreign data set confirmed the great predictive potential of our model. Filtering tests utilizing the decoy test supported the model's additional selective capacity. AUC and ROC values of 0.94 and 1.00 respectively were satisfactory for the constructed model. Atom based 3D-QSAR contour map research exposed the structural constraints for the binding properties of inhibitors against MProinhibitors. Additionally, the outcomes of extra-precision docking demonstrated that the stabilization of the inhibitor within the catalytic pocket is primarily mediated by hydrogen bonding conversations with key binding contaminants Asn42, Asp69, Arg72, Arg132, and Thr163. Hydrophobic interactions were only marginally significant. A computation of binding free energy revealed that van der Waals communication (GvdW), which has a substantial weightage of the van der Waals energy element of the force field OPLS3, is what drives the linkage of inhibitors to the MPro enzyme. This finding is consistent with the rising negative principles of the Glide Emodel. MMGBSA model results are evaluated. MD study three drugs such as Baicalin, MI06 and Benzophenone are discussed. A 100 nsMD study was carried out to look into the specific binding mechanisms between the most effective blocker 107 in the data set and 6XQS. The 107/6XQS complicated MD result and the Glide XP docking outcome correspond rather well. By using in silico pharmacophore-based virtual high-throughput screening, we discovered 5 hits. Depending on the molecular, 3D-QSAR assessment and MD simulation findings, three novel compounds D1-D3 have been suggested as MPro inhibitor. Formulated compounds D1-D3 demonstrated good ADME characteristics.

Acknowledgement

We acknowledge the generous research infrastructure and supports from JSS College of Pharmacy, JSS Academy of Higher Education & Research, Rocklands, Ooty, The Nilgiris, Tamilnadu, India.

Conflicts of interest: The authors declare that they have no conflict of interests

Reference

(1) Raoult, D.; Zumla, A.; Locatelli, F.; Ippolito, G.; Kroemer, G. Coronavirus Infections: Epidemiological, Clinical and Immunological Features and Hypotheses. *Cell stress* **2020**, *4* (4), 66.

(2) Senatore, V.; Zarra, T.; Buonerba, A.; Choo, K.-H.; Hasan, S. W.; Korshin, G.; Li, C.-W.; Ksibi, M.; Belgiorno, V.; Naddeo, V. Indoor versus Outdoor Transmission of SARS-COV-2: Environmental Factors in Virus Spread and Underestimated Sources of Risk. *Euro-Mediterranean journal for environmental integration* **2021**, *6*, 1–9.

(3) ul Qamar, M. T.; Alqahtani, S. M.; Alamri, M. A.; Chen, L.-L. Structural Basis of SARS-CoV-2 3CLpro and Anti-COVID-19 Drug Discovery from Medicinal Plants. *Journal of pharmaceutical analysis* **2020**, *10* (4), 313–319.

(4) Andersen, K. G.; Rambaut, A.; Lipkin, W. I.; Holmes, E. C.; Garry, R. F. The Proximal Origin of SARS-CoV-2. *Nature medicine* **2020**, *26* (4), 450–452.

(5) Bourouiba, L. Turbulent Gas Clouds and Respiratory Pathogen Emissions: Potential Implications for Reducing Transmission of COVID-19. *Jama* **2020**, *323* (18), 1837–1838.

(6) Castano, N.; Cordts, S. C.; Kurosu Jalil, M.; Zhang, K. S.; Koppaka, S.; Bick, A. D.; Paul, R.; Tang, S. K. Fomite Transmission, Physicochemical Origin of Virus–Surface Interactions, and Disinfection Strategies for Enveloped Viruses with Applications to SARS-CoV-2. *ACS omega* **2021**, *6* (10), 6509–6527.

(7) Tang, J. W.; Bahnfleth, W. P.; Bluyssen, P. M.; Buonanno, G.; Jimenez, J. L.; Kurnitski, J.; Li, Y.; Miller, S.; Sekhar, C.; Morawska, L. Dismantling Myths on the Airborne Transmission of Severe Acute Respiratory Syndrome Coronavirus-2 (SARS-CoV-2). *Journal of Hospital Infection* **2021**, *110*, 89–96.

(8) Mousavizadeh, L.; Ghasemi, S. Genotype and Phenotype of COVID-19: Their Roles in Pathogenesis. *Journal of Microbiology, Immunology and Infection* **2021**, *54* (2), 159–163.

(9) Astuti, I. Severe Acute Respiratory Syndrome Coronavirus 2 (SARS-CoV-2): An Overview of Viral Structure and Host Response. *Diabetes & Metabolic Syndrome: Clinical Research & Reviews* **2020**, *14* (4), 407–412.

(10) Thomas, S. The Structure of the Membrane Protein of SARS-CoV-2 Resembles the Sugar Transporter SemiSWEET. *Pathogens and Immunity* **2020**, *5* (1), 342.

(11) Azam, M. A.; Thathan, J.; Jupudi, S. Pharmacophore Modeling, Atom Based 3D-QSAR, Molecular Docking and Molecular Dynamics Studies on Escherichia Coli ParE Inhibitors. *Computational biology and chemistry* **2020**, *84*, 107197.

(12) Giordano, D.; Biancaniello, C.; Argenio, M. A.; Facchiano, A. Drug Design by Pharmacophore and Virtual Screening Approach. *Pharmaceuticals* **2022**, *15* (5), 646.

(13) Cavazzoni, P. Coronavirus (COVID-19) Update: FDA Limits Use of Certain Monoclonal Antibodies to Treat COVID-19 Due to the Omicron Variant. *US Food and Drug Administration* **2022**.

(14) Dahlén, A. D.; Dashi, G.; Maslov, I.; Attwood, M. M.; Jonsson, J.; Trukhan, V.; Schiöth, H. B. Trends in Antidiabetic Drug Discovery: FDA Approved Drugs, New Drugs in Clinical Trials and Global Sales. *Frontiers in Pharmacology* **2022**, *12*, 4119.

(15) Kumar, A.; Rai, S.; Rathi, E.; Agarwal, P.; Kini, S. G. Pharmacophore-Guided Fragment-Based Design of Novel Mammalian Target of Rapamycin Inhibitors: Extra Precision Docking, Fingerprint-Based 2D and Atom-Based 3D-QSAR Modelling. *Journal of Biomolecular Structure and Dynamics* **2021**, *39* (4), 1155–1173.

(16) Bui, T. M.; Butin-Israeli, V.; Wiesolek, H. L.; Zhou, M.; Rehring, J. F.; Wiesmüller, L.; Wu, J. D.; Yang, G.-Y.; Hanauer, S. B.; Sebag, J. A. Neutrophils Alter DNA Repair Landscape to Impact Survival and Shape Distinct Therapeutic Phenotypes of Colorectal Cancer. *Gastroenterology* **2021**, *161* (1), 225–238.

(17) El Aissouq, A.; Toufik, H.; Stitou, M.; Ouammou, A.; Lamchouri, F. In Silico Design of Novel Tetra-Substituted Pyridinylimidazoles Derivatives as c-Jun N-Terminal Kinase-3 Inhibitors, Using 2D/3D-QSAR Studies, Molecular Docking and ADMET Prediction. *International Journal of Peptide Research and Therapeutics* **2020**, *26*, 1335–1351.

(18) El-Hawary, S. S.; Mohammed, R.; Taher, M. A.; AbouZid, S. F.; Mansour, M. A.; Almahmoud, S. A.; Huwaimel, B.; Amin, E. Characterization of Promising Cytotoxic Metabolites from Tabebuia Guayacan Hemsl.: Computational Prediction and In Vitro Testing. *Plants* **2022**, *11* (7), 888.

(19) Zhao, L.-X.; Peng, J.-F.; Liu, F.-Y.; Zou, Y.-L.; Gao, S.; Fu, Y.; Ye, F. Design, Synthesis, and Herbicidal Activity of Diphenyl Ether Derivatives Containing a Five-Membered Heterocycle. *Journal of Agricultural and Food Chemistry* **2022**, *70* (4), 1003–1018.

(20) Ahmad, W.; Ansari, M. A.; Yusuf, M.; Amir, M.; Wahab, S.; Alam, P.; Alomary, M. N.; Alhuwayri, A. A.; Khan, M.; Ali, A. Antibacterial, Anticandidal, and Antibiofilm Potential of Fenchone: In Vitro, Molecular Docking and In Silico/ADMET Study. *Plants* **2022**, *11* (18), 2395.

(21) Liao, S.; Pino Jr, M. J.; Deleon, C.; Lindner-Jackson, M.; Wu, C. Interaction Analyses of hTAAR1 and mTAAR1 with Antagonist EPPTB. *Life Sciences* **2022**, *300*, 120553.

(22) Jupudi, S.; Rajagopal, K.; Murugesan, S.; Kumar, B. K.; Raman, K.; Byran, G.; Chennaiah, J.; pillai Muthiah, V.; Sankaran, S. Identification of Papain-Like Protease Inhibitors of SARS CoV-2 through HTVS, Molecular Docking, MMGBSA and Molecular Dynamics Approach. *South African Journal of Botany* **2022**, *151*, 82–91.

(23) Mitra, N.; Sarkar, P. K.; Prasad, D. Intermolecular Dynamics of Ultraconfined Interlayer Water in Tobermorite: Influence on Mechanical Performance. *Physical Chemistry Chemical Physics* **2019**, *21* (21), 11416–11423.

(24) Zhang, S.; Li, S.; Wei, L.; Zhang, H.; Wang, X.; Liu, B.; Zhang, Y.; Zhang, R.; Qiu, C. Wide-Temperature Tunable Phonon Thermal Switch Based on Ferroelectric Domain Walls of Tetragonal KTN Single Crystal. *Nanomaterials* **2023**, *13* (3), 376.

(25) Tariq, S.; Wani, S.; Rasool, W.; Shafi, K.; Bhat, M. A.; Prabhakar, A.; Shalla, A. H.; Rather, M. A. A Comprehensive Review of the Antibacterial, Antifungal and Antiviral Potential of Essential Oils and Their Chemical Constituents against Drug-Resistant Microbial Pathogens. *Microbial pathogenesis* **2019**, *134*, 103580.

(26) Chang, H.; Tao, Y.; Liaw, P. K.; Ren, J. Phase Prediction and Effect of Intrinsic Residual Strain on Phase Stability in High-Entropy Alloys with Machine Learning. *Journal of Alloys and Compounds* **2022**, *921*, 166149.

(27) Zhang, S.; Wang, N.; Su, L.; Xu, X.; Li, C.; Qin, W.; Zhao, Y. MOA-Based Linear and Nonlinear QSAR Models for Predicting the Toxicity of Organic Chemicals to Vibrio Fischeri. *Environmental Science and Pollution Research* **2020**, *27*, 9114–9125.

(28) Mathpal, D.; Masand, M.; Thomas, A.; Ahmad, I.; Saeed, M.; Zaman, G. S.; Kamal, M.; Jawaid, T.; Sharma, P. K.; Gupta, M. M. Pharmacophore Modeling, Docking and the Integrated Use of a Ligand-and Structure-Based Virtual Screening Approach for Novel DNA Gyrase Inhibitors: Synthetic and Biological Evaluation Studies. *RSC advances* **2021**, *11* (55), 34462–34478.

(29) Ojo, O. A.; Ojo, A. B.; Okolie, C.; Nwakama, M.-A. C.; Iyobhebhe, M.; Evbuomwan, I. O.; Nwonuma, C. O.; Maimako, R. F.; Adegboyega, A. E.; Taiwo, O. A. Deciphering the Interactions of Bioactive Compounds in Selected Traditional Medicinal Plants against Alzheimer’s Diseases via Pharmacophore Modeling, Auto-QSAR, and Molecular Docking Approaches. *Molecules* **2021**, *26* (7), 1996.

(30) Lombino, J.; Gulotta, M. R.; De Simone, G.; Mekni, N.; De Rosa, M.; Carbone, D.; Parrino, B.; Cascioferro, S. M.; Diana, P.; Padova, A. Dynamic-Shared Pharmacophore Approach as Tool to Design New Allosteric PRC2 Inhibitors, Targeting EED Binding Pocket. *Molecular Informatics* **2021**, *40* (2), 2000148.

(31) Liu, Y.; Jiang, Z.; Tong, S.; Sun, Y.; Zhang, Y.; Zhang, J.; Zhao, D.; Su, Y.; Ding, J.; Chen, X. Acidity-Triggered Transformable Polypeptide Self-Assembly to Initiate Tumor-Specific Biomineralization. *Advanced Materials* **2022**, 2203291.

(32) Baillargeon, P.; Robidas, R.; Toulgoat, O.; Michaud, Z.; Legault, C. Y.; Rahem, T. Crystal Structures of Lignocellulosic Furfuryl Biobased Polydiacetylenes with Hydrogen-Bond Networks: Influencing the Direction of Solid-State Polymerization through Modification of the Spacer Length. *Crystal Growth & Design* **2022**, *22* (5), 2812–2823.

(33) Ramachandran, T. S.; Pargunan, K.; Rajasekaran, A.; Kumaran, R. Photophysical Studies on the Interaction of N-Acetyl Tryptophanamide (NATA) With Urea Derivatives in Water.

(34) Grossman, S.; Fishwick, C. W.; McPhillie, M. J. Developments in Non-Intercalating Bacterial Topoisomerase Inhibitors: Allosteric and ATPase Inhibitors of DNA Gyrase and Topoisomerase IV. *Pharmaceuticals* **2023**, *16* (2), 261.

(35) Fang, C.; Ma, H. Ring-Opening Polymerization of Rac-Lactide, Copolymerization of Rac-Lactide and ε-Caprolactone by Zinc Complexes Bearing Pyridyl-Based Tridentate Amino-Phenolate Ligands. *European Polymer Journal* **2019**, *119*, 289–297.

(36) Hudait, A.; Qiu, Y.; Odendahl, N.; Molinero, V. Hydrogen-Bonding and Hydrophobic Groups Contribute Equally to the Binding of Hyperactive Antifreeze and Ice-Nucleating Proteins to Ice. *Journal of the American Chemical Society* **2019**, *141* (19), 7887–7898.

(37) Guo, F.; Zhang, W.; Yang, S.; Wang, L.; Yu, G. 2D Covalent Organic Frameworks Based on Heteroacene Units. *Small* **2023**, 2207876.

(38) Wang, Z.; Pei, Q.; Wang, M.; Tan, J.; Ye, S. Observing Nonpreferential Absorption of Linear and Cyclic Carbonate on the Silicon Electrode. *Langmuir* **2023**, *39* (5), 2015–2021.

(39) Polêto, M. D.; Lemkul, J. A. Integration of Experimental Data and Use of Automated Fitting Methods in Developing Protein Force Fields. *Communications chemistry* **2022**, *5* (1), 38.

(40) Yu, H.; Rouelle, N.; Qiu, A.; Oh, J.-A.; Kempaiah, D. M.; Whittle, J. D.; Aakyiir, M.; Xing, W.; Ma, J. Hydrogen Bonding-Reinforced Hydrogel Electrolyte for Flexible, Robust, and All-in-One Supercapacitor with Excellent Low-Temperature Tolerance. *ACS applied materials & interfaces* **2020**, *12* (34), 37977–37985.

(41) Ren, H.; Zhang, H.; Ni, R.; Li, Y.; Li, L.; Wang, W.; Tian, Y.; Pang, B.; Tan, Y. Detection of Ryanodine Receptor G4911E and I4754M Mutation Sites and Analysis of Binding Modes of Diamide Insecticides with RyR on Galeruca Daurica (Coleoptera: Chrysomelidae). *Frontiers in Physiology* **2022**, *13*, 2685.

(42) Ye, J.; Qi, Y.; Chen, J.; Zhang, S.; Liu, B.; Zhao, Y.; Yuan, X.; Cheng, Q.; Yang, Y.; Zhang, F. Alleviation of Hepatic Steatosis by 4-Azidophlorizin via the Degradation of Geranylgeranyl Diphosphate Synthase by the Ubiquitin-Proteasome Pathway in Vivo and in Vitro. *Advanced Biology* **2023**, 2200150.

(43) Khetan, A. High-Throughput Virtual Screening of Quinones for Aqueous Redox Flow Batteries: Status and Perspectives. *Batteries* **2023**, *9* (1), 24.

(44) Konaklieva, M. I.; Plotkin, B. J. Fragment-Based Lead Discovery Strategies in Antimicrobial Drug Discovery. *Antibiotics* **2023**, *12* (2), 315.

(45) Kalirajan, R.; Pandiselvi, A.; Gowramma, B.; Balachandran, P. In-Silico Design, ADMET Screening, MM-GBSA Binding Free Energy of Some Novel Isoxazole Substituted 9-Anilinoacridines as HER2 Inhibitors Targeting Breast Cancer. *Current Drug Research Reviews Formerly: Current Drug Abuse Reviews* **2019**, *11* (2), 118–128.

(46) Joon, S.; Singla, R. K.; Tjoa, E.; Parmar, K. C.; Shen, B. Alternative Biological Screening Methods. In *Computational Approaches in Drug Discovery, Development and Systems Pharmacology*; Elsevier, 2023; pp 95–137.

(47) Mishra, A.; Maurya, S. K.; Singh, A.; Siddique, H.; Samanta, S. K.; Mishra, N. Neolamarckia Cadamba (Roxb.) Bosser (Rubiaceae) Extracts: Promising Prospects for Anticancer and Antibacterial Potential through in Vitro and in Silico Studies. *Medical Oncology* **2023**, *40* (3), 99.

(48) Zeng, Z.; Guo, P.; Zhang, R.; Zhao, Z.; Bao, J.; Wang, Q.; Xu, Z. Review of Aging Evaluation Methods for Silicone Rubber Composite Insulators. *Polymers* **2023**, *15* (5), 1141.

(49) Huang, C.; Li, S. Computational Molecular Models of Lipid Bilayers Containing Mixed-Chain Saturated and Monounsaturated Acyl Chains. In *Handbook of Nonmedical Applications of Liposomes*; CRC Press, 2023; pp 173–194.

(50) Emmanuel, E.-I. I.; Duke, O. E.; Louis, H.; Gber, T. E.; Undiandeye, U. J.; Imojara, A.; Ikot, I. J. Molecular Modeling of Cu (II), Zn (II), and Hg (II) Metal Complexes of (E)-Benzo [d][1, 3-Dioxol-6-Ylimino) Methyl-4-Bromophenol Schiffbase as Potential Antibacterial Agent. *Chemistry Africa* **2023**, 1–18.

(51) Pavlic, A.; Poelman, H.; Wasilewski, G.; Wichapong, K.; Lux, P.; Maassen, C.; Lutgens, E.; Schurgers, L. J.; Reutelingsperger, C. P.; Nicolaes, G. A. Inhibition of Neutral Sphingomyelinase 2 by Novel Small Molecule Inhibitors Results in Decreased Release of Extracellular Vesicles by Vascular Smooth Muscle Cells and Attenuated Calcification. *International Journal of Molecular Sciences* **2023**, *24* (3), 2027.